

Reflection Modeling of the Black Hole Binary 4U 1630–47: the Disk Density and Returning Radiation

RILEY M. T. CONNORS,¹ JAVIER A. GARCÍA,^{1,2} JOHN TOMSICK,³ JEREMY HARE,⁴ THOMAS DAUSER,²
VICTORIA GRINBERG,⁵ JAMES F. STEINER,^{6,7} GUGLIELMO MASTROSERIO,¹ NAVIN SRIDHAR,⁸ ANDREW C. FABIAN,⁹
JIACHEN JIANG,¹⁰ MICHAEL L. PARKER,¹¹ FIONA HARRISON,¹ AND TIMOTHY R. KALLMAN⁴

¹*Cahill Center for Astronomy and Astrophysics, California Institute of Technology,
Pasadena, CA 91125, USA*

²*Dr Karl Remeis-Observatory and Erlangen Centre for Astroparticle Physics,
Sternwartstr. 7, D-96049 Bamberg, Germany*

³*Space Sciences Laboratory, University of California Berkeley,
7 Gauss Way, Berkeley, CA 94720-7450*

⁴*NASA Goddard Space Flight Center, Greenbelt, MD 20771, USA*

⁵*Institut für Astronomie und Astrophysik, Universität Tübingen, Sand 1, 72076 Tübingen, Germany*

⁶*MIT Kavli Institute, 77 Massachusetts Avenue, 37-241,
Cambridge, MA 02139, USA*

⁷*CfA, 60 Garden St. Cambridge, MA 02138, USA*

⁸*Department of Astronomy, Columbia University,
550 W 120th St, New York, NY 10027, USA*

⁹*Institute of Astronomy, University of Cambridge, Madingley Road, Cambridge CB3 0HA, UK*

¹⁰*Department of Astronomy, Tsinghua University, Shuangqing Road, Beijing 100084, China*

¹¹*European Space Agency (ESA), European Space Astronomy Centre (ESAC), E-28691 Villanueva de la Cañada, Madrid, Spain*

(Accepted by ApJ, 2021 January 15)

ABSTRACT

We present the analysis of X-ray observations of the black hole binary 4U 1630–47 using relativistic reflection spectroscopy. We use archival data from the *RXTE*, *Swift*, and *NuSTAR* observatories, taken during different outbursts of the source between 1998 and 2015. Our modeling includes two relatively new advances in modern reflection codes: high-density disks, and returning thermal disk radiation. Accretion disks around stellar-mass black holes are expected to have densities well above the standard value assumed in traditional reflection models (i.e., $n_e \sim 10^{15} \text{ cm}^{-3}$). New high-density reflection models have important implications in the determination of disk truncation (i.e., the disk inner radius). This is because one must retain self-consistency in the irradiating flux and corresponding disk ionization state, which is a function of disk density and system geometry. We find the disk density is $n_e \geq 10^{20} \text{ cm}^{-3}$ across all spectral states. This density, combined with our constraints on the ionization state of the material, implies an irradiating flux impinging on the disk that is consistent with the expected theoretical estimates. Returning thermal disk radiation—the fraction of disk photons which bend back to the disk producing additional reflection components—is expected predominantly in the soft state. We show that returning radiation models indeed provide a better fit to the soft state data, reinforcing previous results which show that in the soft state the irradiating continuum may be blackbody emission from the disk itself.

Keywords: accretion, accretion disks – atomic processes – black hole physics – 4U 1630-47

1. INTRODUCTION

Black hole X-ray binaries (BHBs) with low-mass companions are known to show transient behavior, with many (8–9) orders of magnitude variation in luminosity during outburst. During such outbursts, BHBs display various states, characterized via several different crite-

ria, most notably the degree of X-ray variability and X-ray spectral properties (see, e.g., Homan & Belloni 2005).

Generally, one can characterize the typical spectral states as follows: hard state, steep power-law state (a part of the broadly classified intermediate state), and thermal-dominated or soft state (see, e.g., Remillard & McClintock 2006). BHBs brighten out of their quiescent phase into the hard state, typically, exhibiting a power-law-like, hard spectrum with $\Gamma \sim 1.5$ –2. The source will then typically transition either directly to the soft, thermal-dominated state, in which a multitemperature blackbody spectrum is typically observed at $kT \sim 1$ keV, or first through the steep power-law state—which lies within the broadly defined intermediate state. The steep power-law state is characterized by comparably strong disk blackbody and power-law emission with a power-law index of $\Gamma \sim 2.5$ –3.

Physical interpretations of the totality of BHB outburst evolution are many, but it is well-established that the general transient nature of BHBs is a result of viscous-thermal instabilities in the accretion flow, known as the disk instability model (DIM; Lasota 2001). The sharp increase in luminosity during an outburst is associated with a rapid increase in the accretion rate \dot{M} of a geometrically thin, optically thick disk progressing from the outer to inner flow. The structure of this accretion disk was originally characterized by Shakura & Sunyaev (1973), emitting strongly as a multitemperature blackbody at high accretion rates. Thus, the intuitive picture of the outburst of a BHB is one of the approach of this thin disk towards the innermost stable circular orbit (ISCO; Novikov & Thorne 1973), which is associated with maximal conversion of gravitational to kinetic/thermal/radiative energy—the thermal-dominated state (McClintock et al. 2006).

Modeling of the reflected X-ray spectra (Ross & Fabian 2005, 2007; García et al. 2014; Dauser et al. 2014) of BHBs has proven a useful tool in our attempts to understand physical changes to the accretion flow across spectral states (see García et al. 2015 and references therein). To this end, recent developments to reflection models have allowed us to make progress in reflection studies (García et al. 2016; Tomsick et al. 2018; Jiang et al. 2019a, Mastroserio et al., in preparation). As the disk density increases beyond the previously assumed value of $n_e = 10^{15} \text{ cm}^{-3}$, additional free-free heating occurs in the upper layers of the disk, leading to a strong quasi-thermal component with a temperature that is proportional to both the density and ionization of the disk (and thus the irradiating flux, since the ionization parameters is given by $\xi = 4\pi F_{\text{irr}}/n_e$, where F_{irr}

is the ionizing flux, and n_e is the disk density; García et al. 2016). High density models have been applied in several recent works to the X-ray spectra of BHBs, showing systematic effects on key physical model parameters (Tomsick et al. 2018; Jiang et al. 2019a). For example, Jiang et al. (2019a) found a weakening of disk truncation constraints when comparing with the very low values found by (Wang-Ji et al. 2018) during the hard state of GX 339–4, though the differences were not large. There has also been success applying the same high-density reflection models to AGN spectra (Jiang et al. 2019b; García et al. 2019).

There is still work needed to characterize the evolution of BHB reflection properties, and their dependence on the disk density, during the transition from the hard to soft states. Recent work has focused on tracking the key accretion flow properties of BHBs with advanced reflection models (e.g., Sridhar et al. 2020; Connors et al. 2020), showing that as BHBs transition from the hard to the soft state, the illuminating continuum may be evolving from a power-law like coronal spectrum to a more disk-blackbody-like spectrum due to the luminosity of the disk. Thus, a comprehensive picture of the evolving accretion flow during transition and into the soft state requires a full treatment of both density effects and the impact of returning disk emission.

4U 1630–47 is one of the most active BHBs to have been observed. Discovered first by the *Vela 5B* satellite in 1969 (Priedhorsky 1986), it has since been detected in outburst > 20 times (Tetarenko et al. 2016). It has a high hydrogen column density along the line of sight, with $N_{\text{H}} \sim (4\text{--}12) \times 10^{22} \text{ cm}^{-2}$ (Kuulkers et al. 1998; Tomsick et al. 1998), with more recent high-resolution X-ray grating spectroscopy with *Chandra* indicating a likely value close to 10^{23} cm^{-2} (Gatuzz et al. 2019). Though the dynamical mass of the BH has not been determined, an indirect mass estimate of $\sim 10 M_{\odot}$ was obtained via scalings of the photon index, Γ , with accretion rate (Seifina et al. 2014). IR observations of its 1998 outburst led to a distance estimate of $D \sim 10$ –11 kpc (Augusteijn et al. 2001; Seifina et al. 2014), and a rough estimate for the orbital period of a few days with an early-type companion star, which is comparatively high. Dips observed in the Proportional Counter Array (PCA; Jahoda et al. 1996) data from the *Rossi X-ray Timing Explorer (RXTE)* showed that the source must have a high binary inclination ($i > 60^\circ$; Tomsick et al. 1998), and later scaling estimates suggest the inclination is probably $< 70^\circ$ (Seifina et al. 2014). Indeed recent reflection modeling showed a preference for an inclination of $\sim 64^\circ$ (King et al. 2014), though this comes with the caveat that reflection spectra depend on the disk incli-

nation, which could in principle be misaligned with the orbital inclination.

4U 1630–47 also exhibits a strong ionized disk wind in the soft state (Kubota et al. 2007; Hori et al. 2014; King et al. 2014; Díaz Trigo et al. 2014; Hori et al. 2018; Gatuuzz et al. 2019), the primary signatures of which are two prominent absorption lines from Fe XXV and Fe XXVI with moderate shifts observed by high-resolution X-ray spectroscopy (provided by observations made by *Chandra*, *XMM-Newton* and *Suzaku*).

In this paper we focus on several different observations of 4U 1630–47, and perform detailed reflection modeling of spectra from the (hard)intermediate to soft states in order to characterize the inner accretion flow during the transition. The key goals are to understand the systematic differences between reflection from low-density and high-density disks. Our focus is primarily on the interplay between the intrinsic disk blackbody and coronal emission, and the reprocessed irradiating flux, a component which depends strongly on density. We use the spectral evolution to constrain this interplay, given the shift in the dominance of the coronal and disk components during the transition.

The structure of this paper as follows: in Section 2 we present all the observations we select for modeling. These include *RXTE*-PCA, the *Nuclear Spectroscopic Telescope Array* (*NuSTAR*; Harrison et al. 2013), and *Neil Gehrels Swift Observatory* (*Swift*; Gehrels et al. 2004). In Section 3 we describe our modeling setup and present results of reflection modeling to PCA and *NuSTAR*/*Swift*-XRT spectra. In Section 4 we discuss the implications of our reflection fitting results and give our conclusions.

2. DATA

We select observations of 4U 1630–47 made by *RXTE*, *NuSTAR*, and *Swift*, specifically its X-ray Telescope (XRT; Krimm et al. 2013). In the following subsections we outline the details of those observations and how we reduced the data.

2.1. *RXTE*

RXTE observed 4U 1630–47 during a total of 9 outbursts between the years of 1996 and 2012, when *RXTE* ceased operating. The short recurrence time and broad coverage with *RXTE* make this a rich dataset, with > 1000 PCA spectra. The full lightcurve and hardness-intensity diagram (HID) are shown in Figure 1. The HID shows that 4U 1630–47 spends the majority of its outbursts in either the soft or intermediate state (including brighter intermediate states akin to the steep power law state, or very high state), which is likely a

Table 1. Properties of the selected *RXTE*-PCA (PCU 2) X-ray spectra from the 1998 and 2002–2004 outbursts of 4U 1630–47.

ObsID	MJD	HR ^a	State ^b	N_{counts}^c (10 ⁶)	cts s ⁻¹ ^d
1998					
30178-01-01-00	50853.1	0.78	Hard	0.3	289
30178-02-01-00	50855.0	0.67	INT	0.9	719
30178-02-01-01	50856.9	0.63	INT	2.6	857
30178-02-02-01	50858.8	0.58	INT	7.9	909
30178-02-13-00	50864.2	0.54	SPL	1.7	1295
30178-01-12-00	50864.6	0.49	SPL	1.9	1181
30188-02-18-00	50868.6	0.46	SPL	4.4	1162
30188-02-19-00	50869.7	0.41	Soft	1.3	765
30172-01-01-00	50883.8	0.32	Soft	3.5	509
2002–2004					
80117-01-03-00G	52795.3	0.60	SPL	18	2392
80117-01-06-00	52802.8	0.63	INT	11	1344
80117-01-07-00	52804.2	0.62	INT	4	1696
80117-01-07-01	52806.5	0.53	SPL	6	2450
80117-01-08-00	52810.1	0.48	SPL	2.2	1685
80117-01-09-01	52816.3	0.36	Soft	2.7	1536
80117-01-13-02	52843.4	0.27	Soft	2.4	1212
80420-01-07-01	52920.9	0.21	Soft	1.0	845
90410-01-03-00	53125.5	0.13	Soft	1.1	490

^a Hardness ratio given by source counts in [8.6–18 keV]/[5–8.6 keV] bands.

^b INT=intermediate, SPL=Steep power law.

^c Number of counts in the 3–45 keV band of the PCU 2 spectra.

^d Total 3–45 keV count rate.

combination of rapid rise times during outburst, and possibly a skew to softer emission due to a hotter, optically thick disk. However, *RXTE* caught 4U 1630–47 in hard and hard-intermediate states during outbursts in 1998 and 2002–2004 (an unusually long and multi-peaked outburst, see Tomsick et al. 2005).

We select data from these two outbursts (see Table 1, and highlighted data in Figure 1) in order to characterize the hard-to-soft transitions of 4U 1630–47, and make direct comparisons with the more recent *NuSTAR* and *Swift* observations. The selection criteria is such that we cover a range of hardness whilst maximizing the total number of detector counts. The key goals of modeling both these datasets are: to constrain the disk density as the source is transitioning; build a consistent picture of the structure of the inner accretion flow during transition; and investigate the key effects the assumption of a higher disk density has on other key disk, coronal, and reflection model parameters.

All the data shown in Table 1 are publicly available on the *RXTE* archive via HEASARC (High Energy Astrophysics Science Archive Research Center). We extracted

Table 2. Properties of the selected *NuSTAR* and *Swift*-XRT spectra.

ObsID	Instr.	MJD	Exp. [ks]	N_{counts}^a (10^6)	cts s $^{-1}$ b
40014009001	<i>NuSTAR</i>	56344	14.7	1.6	112
90002004002	<i>NuSTAR</i>	57073	15.7	2.8	176
90002004004	<i>NuSTAR</i>	57077	16.1	1.8	113
00080510001	<i>Swift</i> -XRT	56344	2.1	0.01	6
00081434001	<i>Swift</i> -XRT	57077	1.6	0.02	14

^a Number of counts in the 3–79 keV band of the *NuSTAR*-FPMA detector, and 0.5–10 keV band of the *Swift*-XRT detector, post-grouping.

^b Mean 3–79 keV (*NuSTAR*) and 0.5–10 keV (*Swift*-XRT) count rates, post-grouping.

the PCA data only, removing data lying within 10 min of the South Atlantic Anomaly (SAA). We use data from proportional counter unit (PCU) 2, due to its superior calibration and extensive coverage (all PCA exposures include PCU 2 data). We corrected the PCU 2 data using the publicly available tool `pcacorr` (García et al. 2014), and introduce 0.1% systematic errors to all channels. The level of systematic errors to impose on the data is based upon the direction of García et al. (2014), showing that the reduction in systematics achieved by the `pcacorr` tool allows one to lower the assumed systematics to $\sim 0.1\%$. We further group the PCU 2 spectra at a signal-to-noise ratio of 4, which achieves sufficient oversampling of the source counts to outweigh the background at high energies. We ignore PCU 2 data in channels 1–4, and beyond 45 keV.

2.2. *NuSTAR* and *Swift*

We use three archival *NuSTAR* observations of 4U 1630-47 taken while the source was in the soft state. *NuSTAR* first observed 4U 1630-47 on UT 2013 February 21 with a total exposure time of 14.7 ks (ObsID 40014009001). The two additional *NuSTAR* observations of 4U 1630-47 taken on 2015 February 20 and 24 (ObsIDs 90002004002 and 90002004004, respectively) have exposure times of 15.7 ks and 16.1 ks respectively. All three *NuSTAR* observations were reduced using version 1.8.0 of the *NuSTAR* Data Analysis Software (NuSTARDAS) package and version 20181030 of the calibration database (CALDB). The *NuSTAR* source spectra for both focal plane modules (FPMA/B) were extracted, using the standard procedures, from an $r = 80''$ circular region centered on the source. The background spectra were extracted from a source-free circular region ($r \approx 70''$) placed on a separate detector chip and avoiding the stray light visible in all three observations.

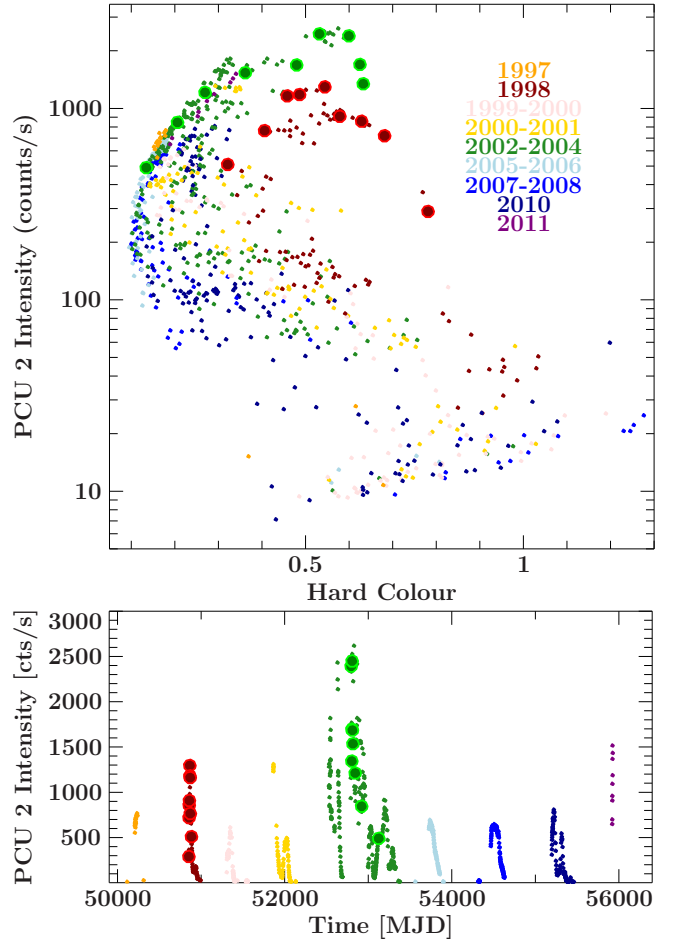


Figure 1. *RXTE*-PCA hardness-intensity diagram (top) and light curve (bottom), including all *RXTE* observations over roughly 10 years—9 outbursts in total. Hard color is defined as the ratio of source counts in the 8.6–18 keV (hard) and 5–8.6 keV (soft) energy bands. The selected observations of outbursts 2 and 5, as shown in Table 1, are highlighted as larger red and green points.

After reducing the data there is some moderate variability remaining (particularly in the first two observations), which may introduce some noisiness in the spectral fits, however, the rms variability on the count rate is on the order of just 10% during each exposure, thus we use the full time-averaged spectra to maximize our statistics. The spectra from all three *NuSTAR* observations were grouped to have a signal-to-noise ratio of at least 10 per energy bin prior to fitting, and we include data only in the 3–79 keV band. The properties of the data are summarized in Table 2.

The *Neil Gehrels Swift*-XRT (Burrows et al. 2005) simultaneously observed 4U 1630-47 with *NuSTAR* on two occasions. The first simultaneous *Swift*-XRT observation (ObsID 00080510001), lasting 2 ks and taken in photon counting (PC) mode, was coincident with *NuSTAR*

TAR ObsID 40014009001. The source spectrum was extracted from an inner annulus between $30''$ – $90''$, while the background spectrum was extracted from an outer annulus between $200''$ – $300''$. The second simultaneous *Swift*-XRT observation (ObsID 00081434001), lasting 1.6 ks and taken in window timing (WT) mode, was coincident with *NuSTAR* ObsID 90002004004. The source spectrum was extracted from an annulus centered on the source having an inner radius of 4 pixels and outer radius of 20 pixels. The inner pixels were excluded from the spectral extraction region to eliminate the effects of pile-up in the PSF core (see e.g., Romano et al. 2006). The background spectrum was extracted from an annulus centered on the source with inner and outer radii of 90 and 110 pixels. *Swift* observation 00081434001 was reduced using HEASOFT version 6.25, observation 00080510001 with HEASOFT version 6.26.1, and both with the x20190412 version of the CALDB. Prior to fitting, the *Swift* spectra were grouped to have a signal-to-noise ratio of at least 10 (00080510001) and 15 (00081434001) per energy bin, and we include data only in the 0.5–10 keV band. The properties of the data are summarized in Table 2.

3. MODELING

Our modeling approach to the multiple *RXTE*-PCA and simultaneous *NuSTAR*/*Swift* data of 4U 1630–47 is as follows. We fit the data with three classes of models, each consisting of a Comptonized multitemperature disk blackbody spectrum plus reflected emission. The distinction is between the nature of the reflected component, and each can be characterized as follows:

- Reflection from a low density disk (fixed to $n_e = 10^{15} \text{ cm}^{-3}$), due to irradiating coronal IC photons.
- Reflection from a disk with variable density (up to $n_e = 10^{22} \text{ cm}^{-3}$), due to irradiating coronal IC photons.
- Reflection of returning disk radiation

The first two models listed are motivated by our goal to test the effects of the disk density on the resultant physical, steady-state characteristics of the accretion flows of BHBs. The dichotomy between the reprocessed quasi-thermal emission of the irradiated upper layers of BHB accretion disks (captured in reflection models which extend to high densities), and the intrinsic disk blackbody emission, has been highlighted in recent works (Zdziarski & De Marco 2020; Zdziarski et al. 2020).

One can make a direct comparison of the disk ionization, ξ , resulting from fitting reflection models, with the

ionization deduced from a rough calculation of the irradiating flux, such that $\xi = 4\pi F_{\text{irr}}/n_e$. We perform these consistency checks with the derived model parameters of our high-density reflection fits. The details of the reflection fits and results are shown in the Section 3.1. All spectral analysis was performed using Xspec, v12.10.1s (Arnaud 1996).

We then investigate the presence of returning radiation in the soft-state observations of *NuSTAR*/*Swift*-XRT by way of a comparison with high-density reflection fits, showing some of the key differences in parameter constraints (Section 3.2).

3.1. *RXTE*-PCA modeling

As outlined in Section 2.1, we selected a subset of PCA observations from outbursts 2 and 5 of 4U 1630–47 (see Figure 1), which occurred in 1998 and 2002–2004. We model these selected spectra with both a low-density and high-density reflection component, as well as a Comptonized disk component.

3.1.1. Model Setup

The models, (a) and (b), are defined explicitly in Table 3. Model (a) represents the standard low-density reflection model, and model (b) is the high-density reflection model. The component **TBabs** accounts for interstellar absorption, implementing the elemental abundance tables of Wilms et al. (2000). We adopt the Verner et al. (1996) atomic cross sections. The **simplcut** component is a model for inverse-Compton (IC) scattering in a coronal plasma (Steiner et al. 2017), and is an extension of the model **simpl** (Steiner et al. 2009b). **simplcut** acts as a convolution model, scattering the disk photons (as described by the multitemperature disk blackbody component **diskbb**; Mitsuda et al. 1984) that traverse hot coronal plasma. It uses the IC spectral calculations given by the Xspec model **nthComp** (Zdziarski et al. 1996; Życki et al. 1999). The temperature of the photon pool for scattering is tied to the **diskbb** value. The parameter f_{sc} sets the proportion of photons which are scattered in the corona. Parameterizing the fraction of photons scattered into the power-law component in this way simplifies the two-part problem: in reality some fraction of photons enter the coronal plasma (a covering fraction), and then some portion of those photons undergo scattering (the optical depth, τ , of the corona sets this quantity). The f_{sc} parameter combines these two quantities, by assuming all photons enter the corona. Thus f_{sc} is a lower bound on the optical depth of the corona, where $\tau \geq -\ln(1 - f_{\text{sc}})$. From a modeling perspective, implementing **simplcut** as a model for IC scattering in a corona is preferable to treating the disk and corona components independently (with their own normalizations)

Table 3. A summary of all models used in spectral fits.

Model	Components
(a)	TBabs(simplcut⊗diskbb+relconvlp⊗reflionx)
(b)	TBabs(simplcut⊗diskbb+relconvlp⊗reflionxHD)
(b.2)	crabcorr*xscat*TBabs(simplcut⊗diskbb + relconv⊗reflionxHD)*xstar
(c)	crabcorr*xscat*TBabs(simplcut⊗diskbb + relxillNS)*xstar

NOTE—`reflionx` and `reflionxHD` differ only in that the latter has a variable disk density, with $n_e \leq 10^{22} \text{ cm}^{-3}$.

because the former enforces self-consistency in the fitting procedure (the coronal IC component can only exist with some total number of disk photons, thus placing limits on the disk flux in the modeling procedure).

Models (a) and (b) are identical in regard to the disk and coronal spectral components, but they differ in the nature of the reflection spectrum. Model (a) assumes a disk density fixed at 10^{15} cm^{-3} . The reflection spectrum is calculated assuming illumination atop the disk by an IC coronal spectrum, as given by the `nthComp` model (Zdziarski et al. 1996; Życki et al. 1999), and thus coincides with the illumination spectrum given by `simplcut⊗diskbb`.

The model `reflionxHD` is the latest version of the long-standing reflection model `reflionx` (Ross & Fabian 2005, 2007), which operates as a grid of reflection spectra which can be implemented in Xspec to perform statistical modeling of X-ray spectra. `reflionxHD` differs from the original `reflionx` model in two key ways: (i) the irradiating continuum ionizing the disk is based on the `nthComp` Comptonization model, as opposed to the approximation of a cutoff power law; (ii) the disk number density is a model parameter extending from 10^{15} cm^{-3} up to 10^{22} cm^{-3} . The model component `relconvlp` is part of the `relxill` distribution of models (García et al. 2014; Dauser et al. 2014) for relativistic reflection, and acts as a convolution model to relativistically smear any input spectrum, assuming a lamppost geometry for the irradiating source. Thus the convolution procedure `relconvlp⊗reflionxHD` applies relativistic smearing to the non-relativistic `reflionxHD` model. We adopt `relconvlp`, the lamppost version of the coronal geometry, based upon previous constraints on the dimensionless BH spin, $a_* = 0.985$, and a steep emissivity, $q > 9$ (King et al. 2014).

3.1.2. Parameters

In all fits to the PCA data shown in Figure 1 and Table 1 we treat the model parameters as follows. Based on explorative preliminary fits to all the data, we fix the hydrogen column density (N_H , a parameter of the `TBabs`

spectral component) to $1.4 \times 10^{23} \text{ cm}^{-2}$. This decision was based on small yet impactful differences between the constrained value of N_H as a function of spectral state and data counts, and an approximate range of values between 1.3 and $1.5 \times 10^{23} \text{ cm}^{-2}$. We further justify this choice due to the uncertainties on N_H in the literature, as measured in the X-ray band (Tomsick et al. 1998; Tomsick & Kaaret 2000; Gattuzz et al. 2019), as well as the presence of dust scattering along the line of sight (Kalemcı et al. 2018). The `simplcut` model has three variable parameters: Γ , the power law photon index, f_{sc} , the scattering fraction, and kT_e , the coronal thermal electron temperature. The `diskbb` component is characterized by the disk normalization N_{disk} , and the inner disk temperature T_{in} . The `reflionxHD` model has parameters for the inner disk temperature T_{in} (this sets the input spectrum for IC scattering, see Jiang et al. 2020, submitted to ApJ), photon index Γ , and electron temperature kT_e —these are all tied to their respective values as given by `simplcut` and `diskbb`. Further `reflionxHD` parameters are disk ionization ξ , iron abundance A_{Fe} , density n_e , and normalization N_{refl} . We fix $A_{\text{Fe}} = 5$ in our fits, again based upon preliminary fits in which typical constrained values were found to be close to 5, with fairly large uncertainties.

The model `relconvlp` has parameters which pertain to the source geometry: the black hole spin a_* , inner disk radius R_{in} , outer disk radius R_{out} , disk inclination i , the lamppost height h , and Γ , the powerlaw index of the IC spectrum. We fix the black hole spin to maximal, $a = 0.998$, and inclination to $i = 64^\circ$, based on the reflection modeling results of King et al. (2014), which also made use of *NuSTAR* observations of the soft state of 4U 1630–47 (observation 40014009001). The inclination constraint also agrees with the lower and upper bounds provided by Tomsick et al. (1998) ($> 60^\circ$) and Seifina et al. (2014) ($< 70^\circ$) respectively. However, we note that there is some evidence that the inner disks of BHBs in general, as probed via reflection modeling, may be misaligned with the outer disk, and thus the orbit in general (see, e.g., Connors et al. 2019). In addition,

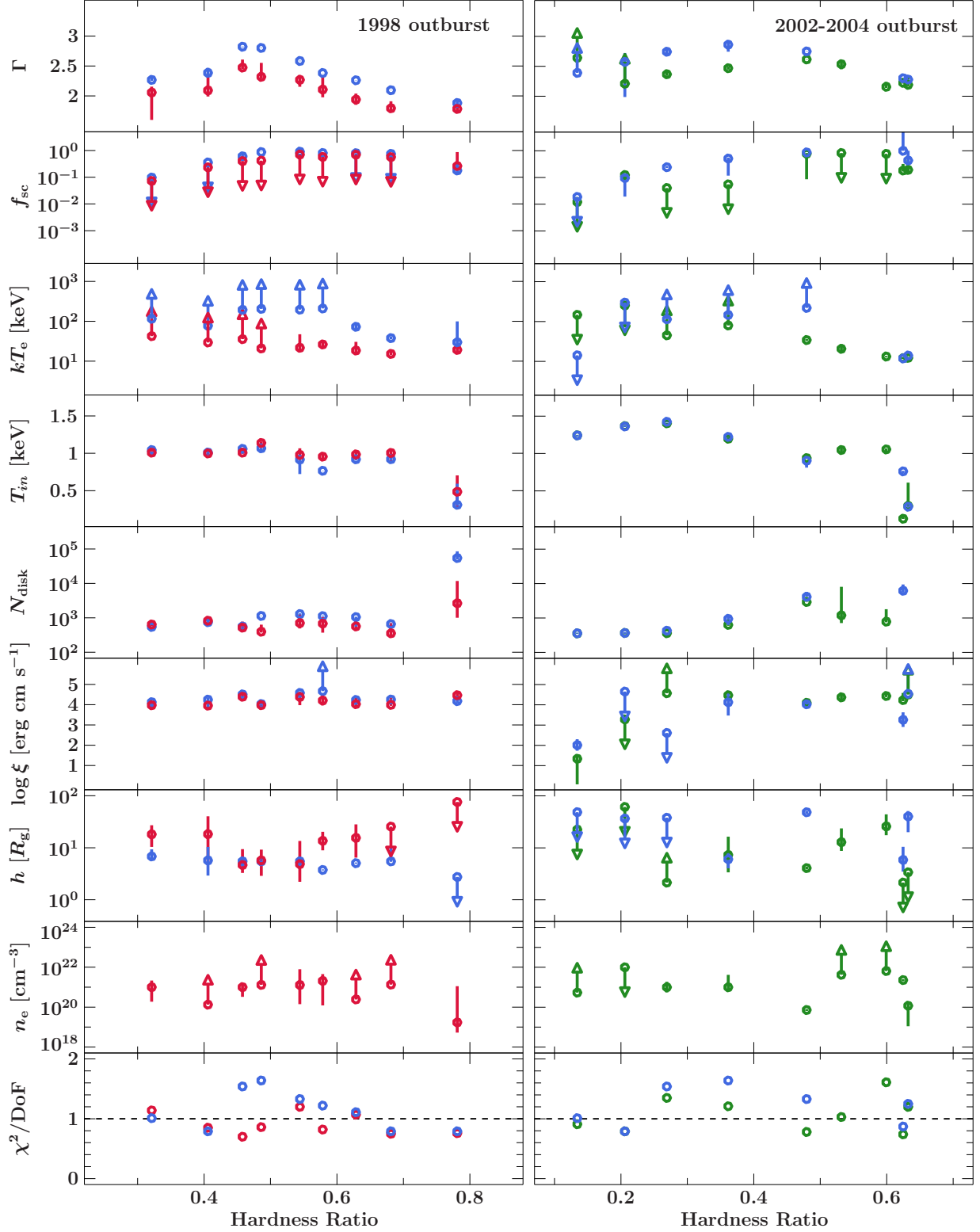


Figure 2. Parameter constraints as a function of hardness ratio resulting from modeling the selected *RXTE*-PCA data from observations of 4U 1630–47 during outbursts in 1998 (left) and 2002–2004 (right). In both plots the blue points show fits of model (a) with $n_e = 10^{15} \text{ cm}^{-3}$. Red and green points show the high-density reflection (Model b) modeling results with data from outbursts in 1998 and 2002–2004 respectively. Observations 80117-01-03-00G and 80117-01-07-01 (hardness ratio 0.60 and 0.53) have no low-density (blue) modeling results included in the right hand panel due to very poor fits to those data.

we fix the inner disk radius to the ISCO ($R_{\text{in}} = R_{\text{ISCO}}$), again based upon preliminary fits which revealed its typical value to be very close to R_{ISCO} , and poorly constrained. Thus, the reflection properties in models (a) and (b) vary only in the disk ionization ξ , the normalization N_{refl} , lamppost height h , and the disk density n_e , which varies freely in model (b)—up to 10^{22} cm^{-3} —but is fixed at low density in model (a). With this carefully curated modeling approach we are able to capture the general differences between low and high density reflection modeling by inspecting the key parameter trends with maximal degrees of freedom in the spectral fits.

Finally, during preliminary fits with both Models (a and b) we also noticed that the PCA detects the well-known Fe XXVI absorption feature at $\sim 6.9 \text{ keV}$, associated with an ionized wind, and previously detected in 4U 1630–47 *NuSTAR* spectra during the soft state (see, e.g., King et al. 2014; Hori et al. 2014). The feature is visible in spectra from the 2002–2004 outburst at hardness ratios below ~ 0.4 (see Figure 1 for reference). As a result, we apply the **gabs** model to those datasets in which the feature is present, in order to factor out those residuals. We fix the centroid energy of the line to 6.9 keV, the Gaussian width to 0.01, and allow only the strength of the line to vary freely.

3.1.3. Spectral Fitting Results

The results of our modeling of the PCA data are summarized visually in Figure 2, with numerical parameter values and their confidence limits presented in Tables 5 and 6 in Appendix A. The first and most fundamental result to highlight is that the disk density, n_e , typically trends towards values $> 10^{20} \text{ cm}^{-3}$ across all spectral states. Secondly, there are some clear and significant differences in the properties of the corona when comparing low and high density reflection models. As the model reaches higher densities, lower values of Γ and kT_e appear to be preferred, particularly during the more intermediate states—this is far clearer in our results for the 1998 outburst data, whereas in our modeling of 2002–2004 the systematic differences are much less obvious, which is likely because the model does not fit as well to those observations. Thus it appears that when higher BHB disk densities are assumed (which is arguably more appropriate based on simple BH mass-scaling arguments, see, e.g., García et al. 2016), one should systematically expect to derive a cooler corona with a harder IC continuum. We discuss the significance of this result in more detail in Section 4.

During the 1998 outburst, in which the source was caught in a harder state, there are clear differences in the disk properties (T_{in} and N_{disk}) between Model (a) and

Model (b), as well as a weaker constraint on the coronal height, h , allowing a lamppost at almost $100 R_g$. The caveat of such statements is that observation 30178-01-01-00 has a low number of counts, and as shown by the reduced χ^2 panel at the bottom of Figure 2, the data are over-fit. Nonetheless, it is curious that the introduction of softer reflected emission due to high-density effects appears to be more consistent with a hotter disk with a smaller inner radius.

We note that Figure 2 does not show results for the low-density reflection modeling of observations 80117-01-03-00G and 80117-01-07-01 (at hardness ratios of 0.60 and 0.53 respectively). This is because the low-density model (Model a) struggles to fit the data within our parameter setup (with the inclination and inner radius frozen). Rather than show results of the improvements we can make to the modeling with additional free parameters, we choose to show the stricter comparisons across hardness.

Figure 2 also shows that generally the disk ionization, presented in log units ($\log[\xi/(\text{erg cm s}^{-1})]$), is ~ 4 , but in the much softer states reached during the 2002–2004 outburst it drops two orders of magnitude to < 2 . This significant decline may not be meaningful because the reflection model dominates the fit over the IC component—thus the constrained value of $\log \xi$ is less reliable, despite the trend coinciding with the drop in coronal flux as expected. In addition, we should expect the bright disk emission to be contributing to the disk ionization, which makes the drop in flux even more suspect. This issue was highlighted in full by Connors et al. (2020), and is possibly evidence that a IC continuum is an inappropriate description of the irradiating continuum in BHB soft states (due to the superior disk flux with respect to the IC emission). We address this in modeling of the *NuSTAR* and *Swift*-XRT data in Section 3.2.

There are not many clear differences in the parameter trends between fits to the 1998 and 2002–2004 outbursts. However, one can notice higher disk temperatures during the 2002–2004 outburst, particularly as the source reached a softer spectral state, where we would expect a higher temperature disk. Constraints on quantities such as the coronal electron temperature, kT_e , scattering fraction, f_{sc} , and coronal height, h , are too weak to properly distinguish the differences between outbursts. The electron temperature kT_e is best constrained in the intermediate states, where we find good agreement between outbursts, despite the doubling in count rate during the latter outburst in 2002–2004 (though as Tables 5 and 6 in Appendix A show, there are slight numerical

differences, with the higher luminosity observations appearing to show a cooler coronal gas).

3.2. *NuSTAR* and *Swift*-XRT modeling

We adopt a similar approach when modeling the *NuSTAR* and *Swift*-XRT data. Here, however, we move on from comparing low and high density modeling, and instead look to compare high-density reflection from coronal illumination of the disk, with the reflected returning disk radiation, following the analysis presented in Connors et al. (2020). In addition, we perform joint spectral modeling, linking key model parameters to better constrain their values across all observations.

3.2.1. Model Setup

The two reflection models we use are `relconv`⊗`reflionxHD` and `relxillNS`. The model `relxillNS` was implemented in Connors et al. (2020), and will be described in detail in a forthcoming paper (Garcia et al., in preparation). It is a variant of the `relxill` consortium of relativistic reflection models (García et al. 2014; Dauser et al. 2014), and behaves similarly to `relxill`, the difference being that the irradiating continuum is a single-temperature blackbody spectrum characterized by kT_{refl} , as opposed to a cutoff power law or IC spectrum.

We use `relxillNS` purely as a consequence of empirical results from modeling, showing that power-law-like reflection proves inadequate during the soft spectral state (Connors et al. 2020). The fundamental driver of this disagreement is the strength of the Compton hump in the reflection component, which is prominent in reflection models which assume an IC irradiating continuum. Reflection from an irradiating blackbody spectrum, on the other hand, naturally results in a weaker Compton hump due to the softer irradiating continuum. The `relxillNS` component acts as a proxy for the reflection spectrum resulting from returning disk radiation illuminating the disk. This is not a model of returning radiation, and the blackbody spectrum we use is a single-temperature one, as opposed to a disk spectrum, so there are strong caveats to using this model. However, it provides us with a way to compare the expected outcome when the disk is reflecting a blackbody-like spectrum as opposed to a power-law-like spectrum.

This model comparison is suitable given how disk-dominated the source was during the *NuSTAR*/*Swift* observations, as shown by simulated data presented in Figure 3, alongside the superior energy resolution of *NuSTAR* (a feature which allows for stricter reflection model comparisons), and the soft X-ray coverage provided by *Swift*-XRT. The simulated PCA observations are based on model fits to the *NuSTAR* spectra where the assumed model is an absorbed Comp-

tonized disk with an absorption line from an ionized wind: `TBabs(simplcut*diskbb)*gabs`. One can see that all three *NuSTAR*/*Swift* observations occurred during the soft state, and basic fits reveal typical disk temperatures of ~ 1.4 keV.

We described the data reduction and grouping in Section 2.2. Here we describe the details of the model treatment and fitting procedure. The first model is similar to Model (b) as presented in Section 3.1, instead now we require additional calibration corrections to fit the *NuSTAR* and *Swift*-XRT spectra simultaneously, as well as the inclusion of dust scattering effects in the model (Kalemcı et al. 2018).

In addition, all the *NuSTAR* spectra clearly display a strong ~ 6.9 keV absorption line, commensurate with a previously confirmed ionized disk wind (Díaz Trigo et al. 2014; King et al. 2014). Given the increased spectral resolution of *NuSTAR* with respect to *RXTE*, we replaced our simplistic Gaussian model for the absorption line with the full, self-consistent `xstar` photoionization model (Kallman & Bautista 2001). We generate a grid of models assuming solar metallicity, and an input blackbody spectrum at a temperature of 1.4 keV, based on initial absorbed disk+powerlaw fits to the simultaneous *NuSTAR* and *Swift*-XRT observations, showing a disk inner temperature of 1.4 keV. We fix the gas density to $n = 10^{15} \text{ cm}^{-3}$, based on typical X-ray wind densities (Miller et al. 2008). We chose an ionizing luminosity of $10^{38} \text{ erg s}^{-1}$, and a turbulent velocity of 1000 km s^{-1} , based upon the variation in its best fit value identified by Díaz Trigo et al. (2014). Typical wind velocities can fall in the range of $300\text{--}3000 \text{ km s}^{-1}$, based upon rough estimates of the Keplerian velocity range corresponding to the radial launching window allowed for thermally driven winds (Ponti et al. 2012). Our grid then has just three variable parameters, the column density, $N_{\text{H,wind}}$, and the ionization, $\log \xi_{\text{wind}}$, and the outflow velocity of the wind, v_{wind} .

The models, now (b.2) and (c), are outlined in Table 3. We replaced the lamppost version of the relativistic convolution model, `relconvlp`, with `relconv`, which instead parameterizes the emissivity profile of irradiation from R_{in} to R_{out} via the index q , where $\epsilon(r) \propto r^{-q}$. This is based on the lack of a lamppost version of the model `relxillNS`, and it therefore allows a more direct comparison of models (b.2) and (c).

The model `crabcorr` (Steiner et al. 2010) applies a correction to the detector response of a given instrument to match the instrument-calibrated normalization and power-law slope of the Crab spectrum (Toor & Seward 1974). Thus its model parameters are N_{CC} and $\Delta\Gamma_{\text{CC}}$, which renormalize and apply a shift in power

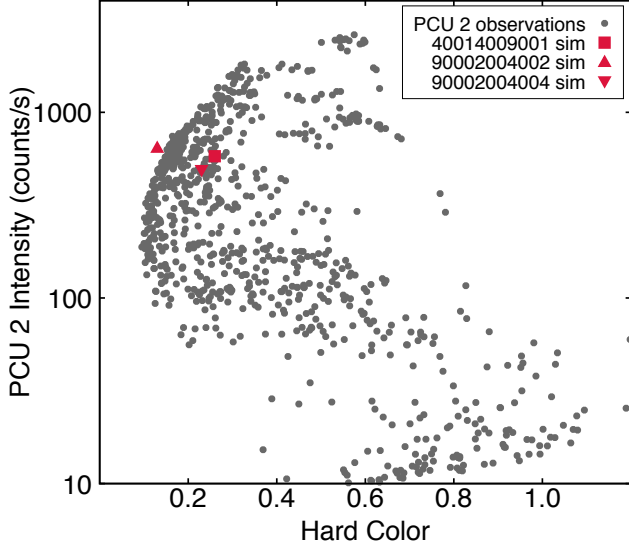


Figure 3. HID showing the archival *RXTE*-PCA (PCU 2) observations of 4U 1630–47 with simulated PCU-2 spectra overplotted. The simulated data are generated from a simple model fit to each of the 3 *NuSTAR* observations of 4U 1630–47. The spectral model used is `TBabs(simplcut@diskbb)*gabs`, and we assume a PCU 2 detector response corresponding to observation 90410-01-03-00 (2002–2004 soft state observation), and an exposure time of 2.5 ks.

law slope respectively. We fix $N_{\text{CC}} = 1$ and $\Delta\Gamma_{\text{CC}} = 0$ in FPM A, and allow only N_{CC} to vary for FPM B. In accordance with the results of Steiner et al. (2010), we apply a $\Delta\Gamma_{\text{CC}} = -0.04$ to the *Swift*-XRT spectra (which are contemporaneous with *NuSTAR* observations 40014009001 and 90002004004). N_{CC} is then left free to vary as a calibration constant for the *Swift*-XRT data relative to *NuSTAR*.

The model `xscat` (Smith et al. 2016) accounts for dust scattering of source photons. For sources with a large hydrogen column density (N_{H}) along the line of sight it is common for a dust scattering halo to form—this is because photons at soft X-ray energies mostly undergo small-angle scattering with dust grains along the line of sight. The effects of dust scattering were explored fully by Kalemci et al. (2018) in the case of 4U 1630–47. They found that the bulk of the dust scattering is likely due to a molecular cloud located close to the source ($\sim 0.94D$, where D is the distance to the source). The `xscat` model implementation in *Xspec* has a few parameters, the most important being X_{pos} , the position of the dust scattering halo along the line of sight to the source, N_{H} , the hydrogen column density of the scattering source (units of 10^{22} cm^{-2}), and R_{ext} , the radius of the circular extraction region in arcseconds. In all our fits we fix $X_{\text{pos}} = 0.9$, $R_{\text{ext}} = 80''$ and $R_{\text{ext}} = 50''$ for the

NuSTAR and *Swift*-XRT spectra respectively. The value of 0.9 for the position of the scatterer is based on the fact that it is likely that multiple scattering regions exist along the line of sight, despite there being a dominant one located at $X_{\text{pos}} = 0.94$ (Kalemci et al. 2018). We then tie N_{H} to the line of sight hydrogen column given by the `TBabs` model. This modeling approach limits the different fits to the same level of dust scattering, as it relates to the interstellar gas absorption (N_{H}).

We perform the spectral fits to all three *NuSTAR* observations (along with the simultaneous *Swift*-XRT observations) jointly, tying model parameters we have *a priori* determined should remain constant. We describe the full parameter setup in the following subsection.

3.2.2. Parameters

Given the superior spectral energy resolution of *NuSTAR* over the PCA, we allow more freedom in the models. We let the iron abundance, A_{Fe} , disk inclination, i , BH spin, a_* , and absorption column density, N_{H} , vary freely, tying them across the three observations such they are assumed to be constant over time. In addition, the disk density, n_{e} , is allowed to vary in model (b.2), again with its value tied across the three observations, given all three are at similar count rates, and disk density is dependent on accretion rate.

As shown by Figure 3, all three observations are during a soft state, and so we assume the thin accretion disk extends to the ISCO ($R_{\text{in}} = R_{\text{ISCO}}$). We let q vary freely in fits with Model b.2, based upon the low- h constraints found in our fits to the PCA data (see Section 3.1). We fix $q = 3$ in our Model c fits, based on preliminary predictions regarding the shallow emissivity profile of returning disk radiation (Wilkins et al. 2020). Whilst `relxillNS` is not itself a physical model of returning radiation—which should be noted as a significant caveat in our spectral fitting approach—the work of Wilkins et al. (2020) shows that the emissivity profile should be flatter than that of a compact corona irradiating the disk. In Model c we also separate the temperature of the irradiating blackbody component from the intrinsic inner disk temperature in `diskbb`: $kT_{\text{refl}} \neq kT_{\text{in}}$. This is based on the inherent uncertainty regarding the relativistic energy shifts experienced by the returning disk photons. We also fix the disk density in `relxillNS` (Model c) to the highest available value the reflection table model affords us, 10^{19} cm^{-3} .

We let the `xstar` parameters vary freely for each individual dataset. These are the wind column density, $N_{\text{H,wind}}$, gas ionization, $\log \xi_{\text{wind}}$, and wind velocity, v_{wind} . The column density parameter has limits in our generated `xstar` table given by 5×10^{21} – 5×10^{23} , and

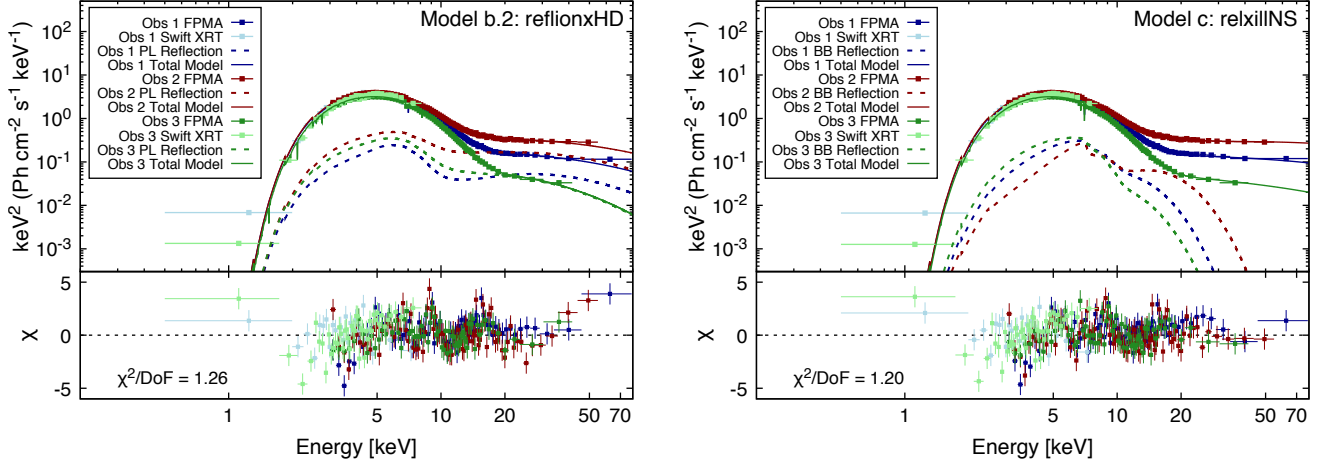


Figure 4. Joint reflection modeling of *NuSTAR* and *Swift*XRT observations of 4U 1630–47 taken in 2013 and 2015. The left panel shows the joint fit of Model (b.2) to all three observations, and the right panel shows fits of Model (c)—descriptions are shown in Table 3. The *xstar* component has been removed from the reflection components to give clarity to the shape of the reflection spectrum. The bottom section of each panel shows the χ standardized residuals—(data–model)/error. *NuSTAR* spectra have been rebinned for plotting at a signal-to-noise ratio of 200 (with a maximum of 5 adjacent bins being combined), and *Swift*-XRT with a signal-to-noise ratio of 20 (again with a maximum of 5 adjacent bin combinations).

the ionization has limits given by 2–5 in log units. The wind velocity is determined by a freely varying redshift parameter on the *xstar* table model.

3.2.3. Spectral Fitting Results

The resulting spectral fits are shown in Figure 4, and corresponding parameters with 90% confidence limits are shown in Table 4. The key result to highlight is that when modeling all three observations Model (c) performs slightly better than Model (b.2). The superiority of reflected returning radiation to fit the broadband X-ray spectra is clear both from the lower total χ^2 for one additional degree of freedom, and the patterns in residuals shown in Figure 4—Model b.2 underfits the high energies and introduces curvature around 10–20 keV. Thus our results make a strong case for returning radiation as a contributor to the observed reflection spectrum in HBB soft states (Connors et al. 2020).

The hydrogen column density is consistently within the range of $9.5\text{--}9.7 \times 10^{22} \text{ cm}^{-2}$, in agreement with recent high-resolution spectroscopic observations with *Chandra* (Gatuzz et al. 2019). The higher value ($14 \times 10^{22} \text{ cm}^{-2}$) assumed in our fits to the PCA data (see Section 3.1) may reflect the increased effects of dust scattering due to the large aperture size of the PCA detectors.

We find that the disk density (when applying Model b.2) exceeds $9 \times 10^{21} \text{ cm}^{-3}$, which is consistent with our findings from modeling of PCA data shown in Section 3.1. However, inspection of Figure 4 also shows that given the source is in the soft state, reflection from illumination of the disk by the corona

(*relconv*⊗*reflionxHD*) tends to over-fit the power law component in the data, introducing an undesirable curvature in the residuals. Indeed the parameter constraints in Table 4 shows this quantitatively in the systematic difference in coronal parameters between Models (b.2) and (c): Model c retrieves similar values of f_{sc} , but significantly lower values of Γ , or in other words a much harder power law component.

The BH spin is high in both Model b.2 and Model c fits, with $a_{\star} = 0.989^{+0.001}_{-0.002}$ and $a_{\star} = 0.85 \pm 0.07$ respectively. The Model b.2 constraint on BH spin thus agrees fairly well with those found by King et al. (2014) in their analysis of the 2013 observations of 4U 1630–47, but the Model c constraint is considerably lower, albeit remaining a high BH spin. This is encouraging given that the models differ slightly, with King et al. (2014) adopting the model *relbhb* (Ross & Fabian 2007) which includes the transmitted emission from internal disk dissipation.

The Model b.2 inclination constraint agrees well with binary orbit inclination limits ($60^\circ < i < 70^\circ$; Tomsick et al. 1998; Seifina et al. 2014), as well as with modeling by King et al. (2014). However, we find a systematic difference in the inclination obtained from Model c (returning radiation) fits, with $i = 37^{+1}_{-2}$ deg. We note that *relxillNS* is a very preliminary model lacking physical consistency, and so we cannot derive much meaning from this difference in inclination. One can speculate that a contrast in inclination with respect to power-law reflection modeling may be expected since there is additional curvature around the Fe line region, as well as a weaker Compton hump—once the reflection line and continuum adjust significantly, one may expect the in-

Table 4. Maximum likelihood estimates of all parameters in spectral fitting of *NuSTAR*/*Swift*-XRT observations of 4U 1630–47, comparing models b.2 and c.

Parameter	Model (b.2)			Model (c)		
	Obs 1	Obs 2	Obs 3	Obs 1	Obs 2	Obs 3
$N_{\text{CC,FPMA}}$				1		
$\Delta\Gamma_{\text{CC,FPMA}}$				0		
$\Delta\Gamma_{\text{CC,FPMB}}$				0		
$\Delta\Gamma_{\text{CC,Swift}}$	–0.04	...	–0.04	–0.04	...	–0.04
$R_{\text{ext},\text{NuSTAR}}$				80''		
$R_{\text{ext},\text{Swift}}$	50''	...	50''	50''	...	50''
$X_{\text{pos,dust}}$				0.9		
kT_e [keV]				300		
R_{in} [R_{ISCO}]				1		
N_{H} [10^{22} cm^{-2}]		$9.49^{+0.04}_{-0.04}$			$9.64^{+0.07}_{-0.06}$	
a_*		$0.989^{+0.001}_{-0.002}$			$0.85^{+0.07}_{-0.07}$	
i [$^\circ$]		$69.7^{+0.4}_{-0.9}$			37^{+1}_{-2}	
A_{Fe} [Solar]		> 4.9			> 9.2	
n_e [10^{20} cm^{-3}]		> 80			0.1 ^a	
Γ	$2.39^{+0.03}_{-0.03}$	$2.21^{+0.02}_{-0.02}$	$2.91^{+0.03}_{-0.04}$	$2.11^{+0.04}_{-0.07}$	$1.94^{+0.02}_{-0.04}$	2.4 ± 0.1
f_{sc}	$0.042^{+0.002}_{-0.003}$	$0.053^{+0.003}_{-0.006}$	< 0.02	$0.038^{+0.004}_{-0.004}$	$0.055^{+0.003}_{-0.004}$	$0.022^{+0.004}_{-0.004}$
kT_{in} [keV]	$1.402^{+0.002}_{-0.003}$	$1.411^{+0.001}_{-0.003}$	$1.397^{+0.002}_{-0.002}$	$1.374^{+0.003}_{-0.008}$	$1.404^{+0.005}_{-0.004}$	$1.398^{+0.008}_{-0.008}$
kT_{refl} [keV]	$2.01^{+0.12}_{-0.08}$	> 2.93	$1.6^{+0.1}_{-0.1}$
N_{disk}	208^{+2}_{-1}	204^{+8}_{-1}	175^{+1}_{-2}	230^{+6}_{-3}	$229.5^{+2.1}_{-0.9}$	173^{+8}_{-3}
q	> 9.8	$9.5^{+0.4}_{-0.3}$	> 9.5	3 ^a	3 ^a	3 ^a
$\log \xi$ [erg cm s ^{–1}]	$2.69^{+0.07}_{-0.07}$	$3.27^{+0.08}_{-0.17}$	$2.90^{+0.02}_{-0.05}$	$3.47^{+0.03}_{-0.31}$	$3.01^{+0.03}_{-0.08}$	$3.2^{+0.3}_{-0.1}$
N_{refl}	$0.61^{+0.05}_{-0.05}$	$0.68^{+0.02}_{-0.03}$	< 0.7	$0.36^{+0.04}_{-0.07} \times 10^{-3}$	$0.34^{+0.04}_{-0.03} \times 10^{-3}$	$0.46^{+0.04}_{-0.03} \times 10^{-3}$
$N_{\text{H,wind}}$ [10^{22} cm^{-2}]	$10.7^{+0.1}_{-3.8}$	$10.7^{+0.1}_{-0.3}$	$2.9^{+0.1}_{-0.1}$	$10.8^{+0.2}_{-3.1}$	$1.9^{+0.6}_{-0.4}$	$10.7^{+0.2}_{-1.3}$
$\log \xi_{\text{wind}}$ [erg cm s ^{–1}]	$4.17^{+0.03}_{-0.18}$	$4.43^{+0.03}_{-0.09}$	$2.57^{+0.05}_{-0.06}$	$4.09^{+0.04}_{-0.04}$	$3.3^{+0.2}_{-0.2}$	$3.90^{+0.04}_{-0.06}$
v_{wind} [km s ^{–1}]	2100^{+600}_{-900}	3000^{+900}_{-1200}	14400^{+300}_{-600}	2100^{+600}_{-600}	12000^{+1000}_{-2000}	1800^{+600}_{-600}
$N_{\text{CC,FPMB}}$	0.955 ± 0.002	$1.015^{+0.001}_{-0.001}$	$1.007^{+0.001}_{-0.002}$	0.955 ± 0.002	1.015 ± 0.001	1.007 ± 0.002
$N_{\text{CC,Swift}}$	1.25 ± 0.02	...	0.823 ± 0.009	1.26 ± 0.02	...	0.824 ± 0.009
χ^2		3080			2938	
ν		2445			2446	
χ^2_ν		1.26			1.20	

NOTE—Model (b.2): `crabcorr*xscat*TBabs(simplcut@diskbb + relconv@reflionxHD)*xstar`. Model (c): `crabcorr*xscat*TBabs(simplcut@diskbb + relxillNS)*xstar`. `xstar` represents the ionized wind, where $N_{\text{H,wind}}$ is the column density of the wind, $\log \xi_{\text{wind}}$ is the wind ionization, and v_{wind} is its outflow velocity. N_{CC} and $\Delta\Gamma_{\text{CC}}$ are the normalization and photon index shifts in the component `crabcorr`, shown in the table for each instrument. R_{ext} is the aperture size assumed to calculate dust scattering in the `xscat` component, and $X_{\text{pos,dust}}$ is the fractional position of the dust scattering halo, where 1 corresponds to the source location. The disk normalization is given by $N_{\text{disk}} = (R_{\text{in}}/\kappa^2 D_{10})^2 \cos i$, where R_{in} is the apparent inner disk in km, D_{10} is the distance to the source in units of 10 kpc, i is the disk inclination, and κ is the color correction factor. The total χ^2 is shown for each fit, along with the degrees of freedom, ν , and the reduced χ^2 , $\chi^2_\nu = \chi^2/\nu$. The ionization, $\log \xi$, is given by $4\pi F_{\text{irr}}/n_e$, where F_{irr} is the ionizing flux, and n_e is the gas density. The normalization definition of the reflection models, given by N_{refl} , is such that the integrated energy flux from 0.1–1000 keV is equal to $10^{20} n_e \xi / 4\pi$. We note however that the density in `relxillNS` (Model c) fits is fixed at 10^{19} cm^{-3} , leading to systematically lower N_{refl} constraints than found via Model b.2 fits with `reflionxHD`.

All other parameters are as described in the text.

^a Frozen parameter

clination to re-adjust to fit the data. We refrain from going beyond this basic explanation, in an effort to avoid speculation on the physical interpretation.

Our ionizing wind parameter constraints reveal a similar dichotomy outlined by King et al. (2014), between ionization state and blueshift of Fe absorption lines. We find that some of our Model/observation combinations (see Table 4) prefer wind velocities on the order of $\sim 2000 \text{ km s}^{-1}$ with higher wind ionization levels, $\log \xi_{\text{wind}}/[\text{erg cm s}^{-1}] \sim 4$. Others prefer an ultra-fast outflow with $v_{\text{wind}} > 10,000 \text{ km s}^{-1}$, and ionizations closer to $\log \xi_{\text{wind}}/[\text{erg cm s}^{-1}] \sim 3$. Whilst the absolute values differ from the results of King et al. (2014), the trends are similar. However, high-resolution spectroscopy provided the best constraints on the disk wind, revealing a relatively low velocity, high ionization, and high column density (Kubota et al. 2007; Díaz Trigo et al. 2014). This is indeed what we find for four of the six model fits. There is no clear and obvious distinction between Models b.2 and c in terms of this dichotomy in the wind properties, so we suggest that the dichotomy is predominantly due to the limiting resolution of the *NuSTAR* spectra compared to, for example, *Chandra* high energy transmission grating (HETG) spectra and *XMM-Newton* spectra. This explains why we King et al. (2014) derived a similar dichotomy.

4. DISCUSSION AND CONCLUSIONS

We have presented detailed reflection modeling of *RXTE*-PCA (Section 3.1), *NuSTAR* and *Swift*-XRT (Section 3.2) observations of 4U 1630–47, exploring a few different physical models for reflection: IC irradiation of both a low and high density accretion disk, and self-irradiation of the disk by returning disk blackbody radiation.

We found that when fitting a reflection model with variable disk density to the PCA observations of 4U 1630–47 one finds densities on the order of 10^{20} cm^{-3} . We also showed that when compared to reflection modeling with a fixed, low density reflector ($n_e = 10^{15} \text{ cm}^{-3}$), the higher density model leads to harder IC spectra with a lower electron temperature—i.e., a cooler Comptonizing corona with a larger optical depth.

4.1. Checking Modeling Consistencies

We can gain some perspective on the consistency of our PCA modeling results via basic calculations of the expected disk ionization as a function of the irradiating flux, as given by the observed coronal IC flux. With this approach, the expected ionization is given by $\xi = 4\pi F_{\text{irr}}/n_e$. The irradiating flux, F_{irr} , is a function of

the disk-corona geometry. The geometry assumed in our modeling is a lamppost corona at some height h , and we assumed a disk extending to the ISCO ($R_{\text{in}} = R_{\text{ISCO}}$). Then the ionization depends on the disk density, n_e , another of our model parameters. Thus this simple expression allows us to confirm whether or not the modeling is consistent with our assumption that the disk is close to the ISCO, as well as place limits on the degree of disk truncation.

Given the degeneracy between the reflected emission and the direct observed coronal emission in the spectral fits, we instead adopt the total 0.1–100 keV unabsorbed disk flux, and multiply by the upper bound f_{sc} value as an approximation of the observed coronal flux (F_{IC}). Assuming an isotropically emitting source, the observed coronal luminosity, L_{irr} , is given by $4\pi D^2 F_{\text{IC}}$, $D = 10.5 \text{ kpc}$. The intrinsic coronal luminosity is then calculated by incorporating relativistic corrections. We then perform full GR ray tracing to calculate the irradiating flux on the disk, assuming a BH mass of $10 M_{\odot}$, and BH spin parameter $a_{\star} = 0.998$. Ray tracing is performed using the *relxill* model in the lamppost geometry (Dauser et al. 2013).

The disk ionization parameter, $\log \xi$, in the *relionxHD* model, is an average disk ionization (it has a fixed value with disk radius). Therefore, the observed disk ionization we determine from fitting the model to data is an average value, while we would expect the actual ionization on the disk to change with the emissivity profile. In order to get an estimate of allowed ionizations that our model predicts, we also calculate the ionization for the radii where the observer sees most of the flux. To be conservative, we use the radii enclosing the area emitting from 10% to 90% of the total observed flux, as counted from the edge of the disk.

Additionally, for the upper ionization limit, we use the lower bound of the lamp post height, and the lower bound of the disk density, n_e , such that we are predicting an absolute upper limit on the irradiating flux and disk ionization state for our model fits. The values are taken from Table 5. Similarly, we also calculate the lower ionization limit, taking respectively the upper limit on the height and disk density.

We show this range and how it compares to the constrained values of $\log \xi$ from the 1998 outburst spectral fits in Figure 5. If the disk sits at the ISCO, particularly during the hardest spectral observation in our sample, the lack of constraint on h means we derive a potential peak disk ionization which exceeds the measured value by 3 orders of magnitude. However, if either the corona is less compact (h is large), or the disk is slightly truncated (out to just $10 R_{\text{ISCO}}$), then the contribution to

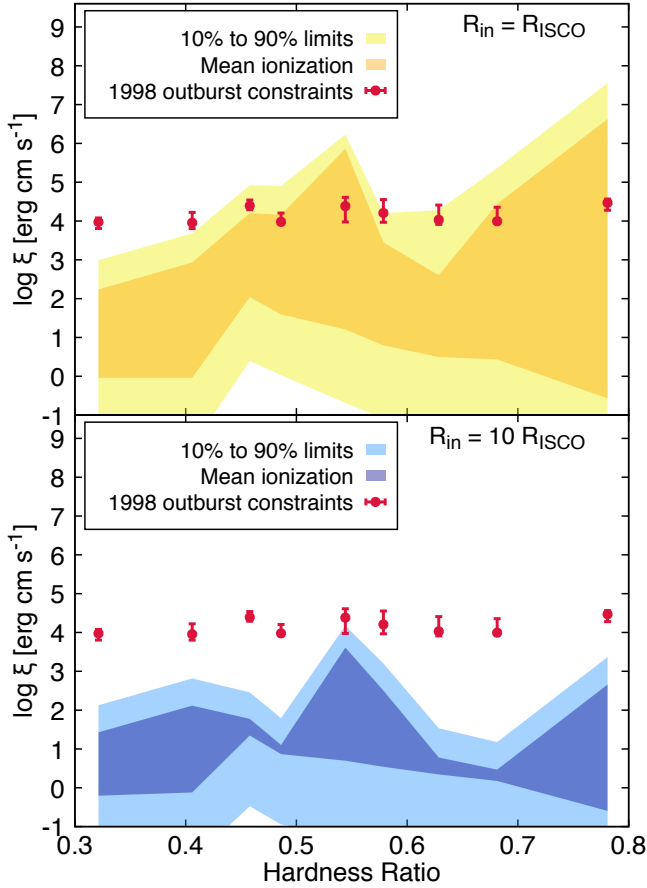


Figure 5. Disk ionization, $\log \xi$, as a function of hardness ratio, showing both the measured values from reflection modeling of the 1998 outburst data (red), and the predicted value given by $\xi = 4\pi F_{\text{irr}}/n_e$ (yellow and blue shaded regions). The top panel shows our predictions for a disk extending to the ISCO, and the bottom panel instead for a disk truncated out to $10 R_{\text{ISCO}}$. Ionizations are calculated for the upper and lower 90% confidence limits on h and n_e , the lamppost height and disk density (see Table 5). The light shaded regions (yellow and blue) show the maximal observed range of disk ionization. This is given by the ionization at the location at which 10% (upper bound) of the total irradiating flux has struck the disk, and then 90% (lower bound). The mean observed ionization (the ionization at the disk radius whereby the disk receives its median flux) is then shown in darker shaded regions (orange and dark blue), again folding in the uncertainty on h and n_e .

the ionization of the disk from coronal illumination sits below the measured value for all values of h . This is actually true of our fits to all 9 spectra, as displayed by the blue shaded region in the bottom panel of Figure 5.

In softer states, when the coronal flux has decreased significantly, we underestimate the constrained disk ion-

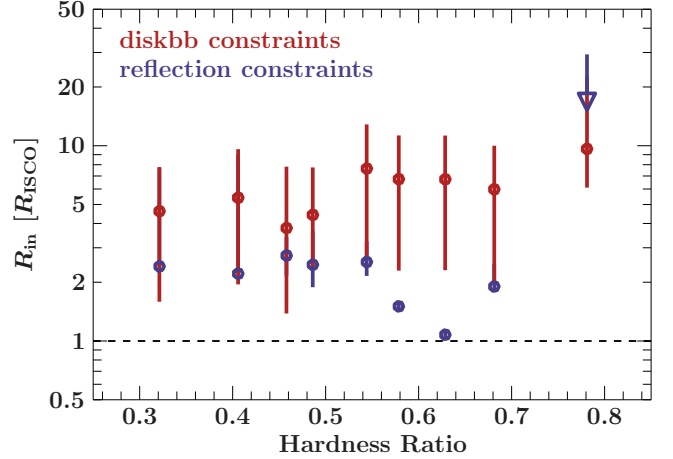


Figure 6. Constraints on the inner disk radius, R_{in} , from both the multi-temperature disk blackbody component (`diskbb`; red) and the relativistic reflection component (`relconv` \otimes `reflionxHD`; blue) as given by model (b) fits to the *RXTE*-PCA 1998 outburst data.

ization. This disagreement may be occurring for several reasons. However, it is most likely a combination of power-law-like reflection being an inappropriate model for the soft state (Connors et al. 2020), as well as a result of neglecting the disk flux, i.e., self-irradiation and heating from the inner regions of the disk, which will contribute significantly to ionizing the upper layers of the disk. Without the data quality to test these degeneracies further, we cannot make any strong statements about inner radius constraints. This simple cross-check instead displays the consistency of key scalings such as disk density and ionizing flux. *Perhaps most importantly, these ionization constraints support the implementation of high-density reflection models in X-ray spectral modeling of BHs.*

In addition to utilizing the disk ionization state as a benchmark for the degree of truncation, one can derive the inner radius directly from the `diskbb` normalization parameter, N_{disk} . We performed the same fits presented in Section 3.1 with two key differences: we fixed the disk density to $n_e = 10^{20} \text{ cm}^{-3}$, and let the inner disk radius, R_{in} , vary freely. This allows us to make a direct comparison between the `diskbb` normalization constraint on R_{in} , as well as constraints from the relativistic reflection component given by `relconv` \otimes `reflionxHD`. The inner disk radius can be derived from the disk normalization parameter as outlined by Mitsuda et al. (1984), whereby $R_{\text{in}} [\text{km}] = \kappa^2 D_{10} (N_{\text{disk}} / \cos i)^{1/2}$, where κ is the color correction factor (Kubota et al. 1998), D_{10} is the distance to the source in units of 10 kpc, and i is the disk inclination. We assume a fixed disk inclination of 64° as in the spectral fits presented in Section 3.1, and we

adopt the best fit N_{disk} values with their uncertainties. We then assume a nominal value for the color correction of $\kappa = 1.5$, and allow for values between 1 and 2. We then propagate the uncertainties on both N_{disk} and κ to calculate R_{in} and its uncertainties. Figure 6 shows the comparison of disk and reflection constraints on R_{in} in units of R_{ISCO} .

The large uncertainties on R_{in} predictions derived from the N_{disk} constraints are largely due to the uncertainty on the color correction factor ($1 \leq \kappa \leq 2$). With these uncertainties incorporated into the predicted values, just two of the nine disk and reflection R_{in} predictions disagree, and only on the order of R_{ISCO} , all within an order of magnitude. Thus our results reinforce recent work presenting a near identical type of parametric comparison applied to BHB GX 339–4 presented by Sridhar et al. (2020). The remarkable agreement between the expected size of the blackbody emitting disk (i.e. its inner radius) and the reflection constraint is encouraging in terms of the validity of the high-density reflection models for explaining the system properties. This connection, along with the consistency of our predicted ionizations with the measured value from reflection modeling, suggests we are arriving at an accurate physical representation of 4U 1630–47 and its accretion flow properties.

We have also shown that in the soft state the reflection spectrum likely has a contribution from returning disk radiation. Our fits of the `relxillNS` model to the *NuSTAR*/*Swift*-XRT data are superior to those made with `relionxHD`, which assumes the irradiating continuum is purely from a Comptonizing medium. A further consistency check provides us with supporting evidence for the presence of reflected returning disk radiation. The unabsorbed coronal IC fluxes derived from our Model c fits (Section 3.2) are $3 \times 10^{-10} \text{ erg s}^{-1} \text{ cm}^{-2}$, $7 \times 10^{-10} \text{ erg s}^{-1} \text{ cm}^{-2}$ and $3 \times 10^{-11} \text{ erg s}^{-1} \text{ cm}^{-2}$ respectively. These fluxes are a mere 2%, 3% and 0.2 % of the total source flux respectively. In addition, the fractional flux (of the total) of the reflection components `relxillNS` are 4%, 4%, and 8% respectively—we note that these estimates are derived using the best fit parameters, not the full confidence regions. Connors et al. (2020) showed that we would typically expect $\sim 5\%$ of emitted disk photons to return to strike the disk for a black hole spin of 0.5. Here we obtain relatively high BH spin ($a_* = 0.85 \pm 0.07$). In this case, the fraction of returning radiation can be several factors higher (Connors et al. 2020; Wilkins et al. 2020).

Thus our spectral fitting results are consistent with predictions for maximally spinning BHs whereby the inner disk lies within a few R_g of the BH. There are

strong caveats to this calculation though, since `relxillNS` is not a physical model of returning radiation, and thus far we are relying on ray tracing of returning disk radiation which yields a *photon flux striking the disk* (Wilkins et al. 2020), not an *observed energy flux*, which is what we have derived from the fits. Therefore we stress that we only make this simple comparison to indicate that it may be reasonable to expect fluxes on the order of $\sim 10\%$ in the reflected returning radiation component. Further tests are required to verify these numbers with full calculations of energy shifts in the returning disk emission, and this is work that is currently ongoing (Dauser et al., in preparation).

It is worth comparing the results of reflection modeling of the *NuSTAR* observations with that of the *RXTE* observations presented in Section 3.1. Specifically, what impact would the inclusion of returning radiation (represented by the model `relxillNS`) have on the parameter constraints we derived under the assumption of purely coronal disk illumination? Table 4 shows that returning radiation can have an appreciable contribution to the total observed flux, and explain reflection features, when the source has a relatively minimal contribution from IC flux (with $f_{\text{sc}} \leq 0.1$). Tables 5 and 6 show we may expect returning radiation to contribute significantly once the source drops to hardness ratios below ~ 0.4 . Inclusion of the returning radiation component as the dominant reflector would likely result in lower values of the IC photon index, Γ , and potentially a necessary adjustment of the disk inclination. It is also possible we would necessarily have to adjust the BH spin, though this is difficult to predict without performing the fits.

Finally, the constraints from reflection fitting imply a superabundance of iron in the disk, whereas we have assumed the disk wind has solar iron abundance (`XSTAR`). Whilst this could skew our results, we note that the implied high abundances of iron in accretion disks via reflection modeling is still in the process of being understood (see, e.g., García et al. 2018).

4.2. Comparisons with Previous Work

King et al. (2014) presented reflection modeling of the same 2013 *NuSTAR* observation of 4U 1630–47. However, they adopted the model `refbhb` (Ross & Fabian 2007; Reis et al. 2008), which accounts for the underlying blackbody emission of the disk propagating through the ionized upper layers of the disk. This has some similarities with reflected returning radiation, but there is a clear physical distinction. Thus it is difficult to make direct comparisons. However, our results are broadly consistent with those of King et al. (2014), both in terms of the disk and coronal continuum parameters, and some

key reflection parameters. For example we generally constrain the disk inclination to be in the range 60° – 70° in high-density reflection fits, though we note that in our fits it was necessary to allow the emissivity index q to vary freely. We also find similar disk density constraints ($\geq 10^{21} \text{ cm}^{-3}$). The difference in disk temperature (King et al. 2014 find $kT_{\text{in}} \sim 1 \text{ keV}$) likely occurs because King et al. (2014) adopt a reflection model which includes intrinsic underlying disk emission in the `refbhb` model. Indeed King et al. (2014) find a similar disk temperature of 1.45 keV when employing a simpler disk+power law model.

Our joint spectral fits to the joint *NuSTAR*/*Swift*-XRT observations during the soft state revealed that reflection from a disk blackbody performed better than reflection from a power law component. This echoes previous results found by Díaz Trigo et al. (2014). Direct comparison to their results is difficult, because they compare the `relxill` model with a model which convolves any input continuum and performs the reflection calculation, `rfxconv` (Kolehmainen et al. 2011). Díaz Trigo et al. (2014) suggest, however, that the observed reflection features originate in the interaction of the disk emission with the ionized wind component, as opposed to reflection of photons off the disk (returning radiation). The rationale for this suggestion originates in the correlation between the strength of reflection features—such as Fe line equivalent width, and reflection fraction—and the column density of the warm absorber. This is a plausible explanation for the observed features, as has been found by recent works, e.g., Higginbottom et al. (2020). Including these potential scattering and line emission effects in the warm absorber could affect our reflection modeling results, as such processes may mimic some of the reflection features, in particular the Fe line emission and Compton hump. Addressing these effects requires a much larger effort well outside the scope of this paper.

Tomsick et al. (2005) explored *RXTE* observations of the 2002–2004 outburst of 4U 1630–47, noting the extreme behaviors of 4U 1630–47 during transition to the soft state, and postulating that the source is close to the Eddington limit. They found that the inner disk temperature, kT_{in} , varied between 2.7 and 3.8 keV during flaring in the intermediate state. The results presented in this work shed more light on the nature of the inner disk emission when reprocessing of coronal IC irradiation of a high-density disk is accounted for. As noted by Tomsick et al. (2005), as the source exceeds $0.2L_{\text{Edd}}$, electron scattering in the inner flow can heat the disk to such high temperatures. However, the effects of increased disk density are similar, with free-free heating increasing the temperature of the upper layers of

the disk (García et al. 2016). Thus these two processes are degenerate, which may partially explain the lower disk temperatures derived in our fits to the 2002–2004 PCA observations—high-density reflection effects subsume some of the strong high-temperature disk emission discussed by Tomsick et al. (2005). However, it should be noted that we are likely also deriving lower disk temperatures in the bright intermediate states due to the IC component we adopt (`simplcut`⊗`diskbb`), as opposed to the disconnected approach taken by Tomsick et al. (2005) (`diskbb`+`powerlaw`). The former approach, which we took here, leads to lower disk temperatures due to the suppression of softer powerlaw flux when photon conservation is applied, as opposed to letting the power law fit independently of the disk (see Steiner et al. 2009a for a full discussion).

Several recent articles have focused on high-density reflection modeling (e.g., Tomsick et al. 2018; Jiang et al. 2019a). Unlike Tomsick et al. (2018), who compared low density to high density reflection modeling of the BHB Cyg X-1, we do not find strong evidence for a reduction in iron abundance constraints when adopting high density reflection models. This is in part due to the low statistical quality of the PCA data (we fixed $A_{\text{Fe}} = 5$ in all our fits), but applies to modeling of *NuSTAR*/*Swift*-XRT as well. Table 4 shows that in our joint spectral fits, Model b.2 gives $A_{\text{Fe}} > 4.9$, close to the upper limit of the `reflionxHD` model.

Jiang et al. (2019a) fit high-density reflection models to *NuSTAR* and *Swift* observations of GX 339–4 during a relatively low-flux hard state and a bright soft state. They found disk densities in the lowest-flux hard state of $\sim 10^{21} \text{ cm}^{-3}$, and $\sim 10^{19} \text{ cm}^{-3}$ during a brighter soft state observation. We are not able to comment on the distinction between low-flux hard states and the soft state in our fits to 4U 1630–47, simply because of lack of good observational coverage of its rapid rise and transition.

4.3. Conclusions

Two key conclusions arise from our results. Firstly, high-density modeling of the BHB 4U 1630–47 shows an improved consistency in the scalings of ionizing coronal IC flux and the corresponding disk ionization state given by the reflection model (in contrast to low-density reflection models). Secondly, echoing previous results found by Connors et al. (2020) and Wilkins et al. (2020), during BHB soft states the irradiating continuum and resulting reflection component may be more like a reflected blackbody spectrum as opposed to reflection of the less dominant IC component.

We recommend exploring high-density reflection modeling of more sources, preferably in the bright hard state, with instruments such as *NuSTAR* and the *Neutron Star Interior Composition Explorer (NICER)*, providing broadband X-ray coverage, sensitivity to the soft emission, and high spectral resolution. We need to build a large sample of such results in order to make broad comparisons with previous results using low-density reflection models. In addition, similar to the approach taken in this paper, one should check their reflection modeling results for consistency—the scalings of irradiating flux and the fit value of disk ionization should be consistent.

Finally, in future work we will present more detailed models for returning radiation that are physically self-consistent (i.e., full relativistic ray tracing of returning photons from the disk, Dauser et al., in preparation). More self-consistent models will allow us to test the validity of returning radiation as a dominant reflection component, since the fraction and spectral shape of the returning photons depends strongly on BH spin and system geometry.

We thank the referee for their comments, each of which facilitated the improvement of this manuscript.

This work was partially supported under NASA contract No. NNG08FD60C and made use of data from the *NuSTAR* mission, a project led by the California Institute of Technology, managed by the Jet Propulsion Laboratory, and funded by the National Aeronautics and Space Administration. We thank the *NuSTAR* Operations, Software, and Calibration teams for support with

the execution and analysis of these observations. This research has made use of the *NuSTAR* Data Analysis Software (NuSTARDAS), jointly developed by the ASI Science Data Center (ASDC, Italy) and the California Institute of Technology (USA).

R.M.T.C. has been supported by NASA ADAP grant 80NSSC177K0515. J.A.G. acknowledges support from NASA APRA grant 80NSSC17K0345 and from the Alexander von Humboldt Foundation. VG is supported through the Margarete von Wrangell fellowship by the ESF and the Ministry of Science, Research and the Arts Baden-Württemberg. JAT acknowledges partial support from NASA ADAP grant 80NSSC19K0586.

This research has made use of data, software and/or web tools obtained from the High Energy Astrophysics Science Archive Research Center (HEASARC), a service of the Astrophysics Science Division at NASA/GSFC and of the Smithsonian Astrophysical Observatory’s High Energy Astrophysics Division.

This research has made use of ISIS functions (ISIScripts) provided by ECAP/Remeis observatory and MIT (<http://www.sternwarte.uni-erlangen.de/isis/>).

Facilities: *RXTE* (PCA; [Jahoda et al. 1996](#)), *NuSTAR* ([Harrison et al. 2013](#)), *Swift*-XRT ([Krimm et al. 2013](#)), HEASARC

Software: XSPEC v.12.10.1s ([Arnaud 1996](#)), RELIONX ([Ross & Fabian 2005, 2007](#)), XILLVER ([García & Kallman 2010; García et al. 2013](#)), RELXILL (v1.3.3; [García et al. 2014; Dauser et al. 2014](#)), PCACORR ([García et al. 2014](#)).

APPENDIX

A. PCA SPECTRAL FITTING RESULTS

Tables 5 and 6 show the numerical parameter constraints from fits of Models a and b to PCA observations of 4U 1630–47 during 1998 and 2002–2004. The results of this analysis are discussed in detail in Section 3.1, and the values shown in Tables 5 and 6 correspond to the parameter trends shown in Figure 2, but with some small distinctions due to rounding of errors.

REFERENCES

- Arnaud, K. A. 1996, in *Astronomical Society of the Pacific Conference Series*, Vol. 101, *Astronomical Data Analysis Software and Systems V*, ed. G. H. Jacoby & J. Barnes, 17
- Augusteijn, T., Kuulkers, E., & van Kerkwijk, M. H. 2001, *A&A*, 375, 447, doi: [10.1051/0004-6361:20010855](https://doi.org/10.1051/0004-6361:20010855)
- Burrows, D. N., Hill, J. E., Nousek, J. A., et al. 2005, *SSRv*, 120, 165, doi: [10.1007/s11214-005-5097-2](https://doi.org/10.1007/s11214-005-5097-2)
- Connors, R. M. T., García, J. A., Steiner, J. F., et al. 2019, *ApJ*, 882, 179, doi: [10.3847/1538-4357/ab35df](https://doi.org/10.3847/1538-4357/ab35df)
- Connors, R. M. T., García, J. A., Dauser, T., et al. 2020, *ApJ*, 892, 47, doi: [10.3847/1538-4357/ab7afc](https://doi.org/10.3847/1538-4357/ab7afc)
- Dauser, T., García, J., Parker, M. L., Fabian, A. C., & Wilms, J. 2014, *MNRAS*, 444, L100, doi: [10.1093/mnras/llu125](https://doi.org/10.1093/mnras/llu125)
- Dauser, T., Garcia, J., Wilms, J., et al. 2013, *MNRAS*, 430, 1694, doi: [10.1093/mnras/sts710](https://doi.org/10.1093/mnras/sts710)
- Díaz Trigo, M., Migliari, S., Miller-Jones, J. C. A., & Guainazzi, M. 2014, *A&A*, 571, A76, doi: [10.1051/0004-6361/201424554](https://doi.org/10.1051/0004-6361/201424554)

Table 5. Maximum likelihood estimates of all parameters in spectral fitting of *RXTE*-PCA observations of the 1998 outburst of 4U 1630–47 with models (a) and (b). Model (a) enforces a fixed low-density reflection component ($n_e = 10^{15} \text{ cm}^{-3}$), and model (b) has a variable disk density with $n_e \leq 10^{22} \text{ cm}^{-3}$.

Parameter	Hardness Ratio								
	0.78	0.67	0.63	0.58	0.54	0.49	0.46	0.41	0.32
$R_{\text{in}} [R_{\text{ISCO}}]$	1								
a_*	0.998								
$i [^\circ]$	64								
A_{Fe}	5								
$N_{\text{H}} [10^{22} \text{ cm}^{-2}]$	14								
Model (a): TBabs(simplcut⊗diskbb+relconvlp⊗reflionx)									
Γ	$1.88^{+0.04}_{-0.03}$	$2.095^{+0.002}_{-0.003}$	$2.262^{+0.002}_{-0.003}$	$2.3828^{+0.0015}_{-0.0007}$	$2.584^{+0.004}_{-0.004}$	$2.802^{+0.004}_{-0.003}$	$2.822^{+0.001}_{-0.010}$	$2.39^{+0.08}_{-0.04}$	$2.27^{+0.05}_{-0.02}$
f_{sc}	$0.18^{+0.13}_{-0.06}$	< 0.74	< 0.80	$0.806^{+0.006}_{-0.001}$	$0.905^{+0.007}_{-0.096}$	$0.876^{+0.017}_{-0.005}$	$0.6^{+0.1}_{-0.2}$	< 0.4	< 0.1
$T_{\text{in}} [\text{keV}]$	$0.31^{+0.28}_{-0.01}$	$0.92^{+0.02}_{-0.02}$	$0.92^{+0.02}_{-0.02}$	$0.766^{+0.002}_{-0.003}$	$0.916^{+0.005}_{-0.193}$	$1.068^{+0.005}_{-0.054}$	$1.059^{+0.017}_{-0.009}$	$1.01^{+0.01}_{-0.02}$	$1.044^{+0.005}_{-0.005}$
$kT_{\text{e}} [\text{keV}]$	30^{+70}_{-8}	38^{+4}_{-3}	70^{+10}_{-10}	> 210	> 200	> 200	> 200	> 100	> 100
$N_{\text{disk}} [10^2]$	550^{+310}_{-50}	$6.6^{+0.1}_{-0.1}$	$10.5^{+0.2}_{-5.0}$	$11.2^{+0.4}_{-0.4}$	$12.8^{+0.7}_{-0.6}$	$11.4^{+0.1}_{-0.2}$	$5.58^{+0.07}_{-0.41}$	7^{+3}_{-1}	$5.4^{+0.2}_{-0.1}$
$h [R_{\text{g}}]$	< 2.7	$5.5^{+5.1}_{-0.1}$	$5.0^{+0.1}_{-0.1}$	$3.75^{+0.08}_{-0.09}$	$5.5^{+0.3}_{-0.3}$	$5.5^{+0.2}_{-0.2}$	$5.48^{+1.02}_{-0.06}$	6^{+5}_{-3}	$6.8^{+2.5}_{-0.9}$
$\log \xi [\text{erg cm s}^{-1}]$	$4.18^{+0.18}_{-0.08}$	$4.26^{+0.02}_{-0.03}$	$4.23^{+0.03}_{-0.03}$	> 4.65	$4.58^{+0.08}_{-0.08}$	$4.03^{+0.04}_{-0.07}$	$4.51^{+0.04}_{-0.03}$	$4.25^{+0.09}_{-0.36}$	$4.13^{+0.02}_{-0.09}$
$N_{\text{refl}} [10^3]$	$9.9^{+0.9}_{-3.0}$	$1.74^{+3.08}_{-0.04}$	$2.38^{+0.09}_{-0.09}$	$6.22^{+0.09}_{-0.10}$	$4.7^{+2.4}_{-0.2}$	$5.6^{+34.7}_{-0.3}$	$7.41^{+2.17}_{-0.05}$	3^{+9}_{-2}	$1.4^{+5.9}_{-0.6}$
$n_{\text{e}} [\text{cm}^{-3}]$	10^{15}								
χ^2	54	56	79	86	91	81	122	62	85
ν	68	71	71	71	68	68	69	66	67
χ^2_{ν}	0.79	0.79	1.11	1.22	1.33	1.19	1.76	0.94	1.27
Model (b): TBabs(simplcut⊗diskbb+relconvlp⊗reflionxHD)									
Γ	$1.78^{+0.05}_{-0.06}$	$1.79^{+0.12}_{-0.05}$	$1.94^{+0.10}_{-0.09}$	$1.88^{+0.04}_{-0.03}$	$2.27^{+0.08}_{-0.12}$	$2.32^{+0.23}_{-0.03}$	$2.47^{+0.13}_{-0.03}$	$2.1^{+0.3}_{-0.1}$	$2.1^{+0.1}_{-0.5}$
f_{sc}	< 0.9	< 0.6	< 0.7	< 0.6	< 0.7	< 0.4	< 0.4	< 0.2	< 0.07
$T_{\text{in}} [\text{keV}]$	$0.5^{+0.2}_{-0.2}$	$1.01^{+0.03}_{-0.11}$	$0.98^{+0.05}_{-0.07}$	$0.96^{+0.05}_{-0.05}$	$0.98^{+0.09}_{-0.07}$	$1.14^{+0.02}_{-0.07}$	$1.01^{+0.02}_{-0.02}$	$1.00^{+0.02}_{-0.04}$	$1.009^{+0.023}_{-0.008}$
$kT_{\text{e}} [\text{keV}]$	19^{+6}_{-3}	15^{+3}_{-1}	18^{+12}_{-4}	26^{+6}_{-4}	22^{+26}_{-5}	> 30	> 30	> 30	> 40
$N_{\text{disk}} [10^2]$	30^{+90}_{-20}	$3.5^{+3.6}_{-0.5}$	6^{+3}_{-1}	7^{+4}_{-3}	7^{+6}_{-2}	$3.9^{+2.4}_{-0.2}$	$5.2^{+2.5}_{-0.4}$	$8.2^{+2.6}_{-0.6}$	$6.4^{+0.2}_{-0.6}$
$h [R_{\text{g}}]$	< 100	< 20	15^{+13}_{-9}	14^{+7}_{-5}	5^{+9}_{-3}	6^{+3}_{-3}	5^{+5}_{-1}	20^{+20}_{-10}	18^{+9}_{-8}
$\log \xi [\text{erg cm s}^{-1}]$	$4.47^{+0.09}_{-0.19}$	$3.99^{+0.36}_{-0.05}$	$4.0^{+0.4}_{-0.1}$	$4.2^{+0.3}_{-0.2}$	$4.4^{+0.2}_{-0.4}$	$3.98^{+0.23}_{-0.06}$	$4.4^{+0.1}_{-0.1}$	$4.0^{+0.3}_{-0.2}$	$4.0^{+0.1}_{-0.2}$
N_{refl}	$2.0^{+2.3}_{-0.7}$	$1.8^{+0.6}_{-0.8}$	$2.2^{+0.8}_{-0.6}$	$2.9^{+1.0}_{-0.7}$	6^{+13}_{-3}	$3.7^{+2.0}_{-0.8}$	$6.4^{+2.4}_{-0.9}$	$2.0^{+1.6}_{-0.9}$	$1.3^{+1.6}_{-0.3}$
$n_{\text{e}} [10^{20} \text{ cm}^{-3}]$	$0.2^{+11.0}_{-0.1}$	> 10	> 2	21^{+24}_{-19}	13^{+66}_{-11}	> 10	10^{+4}_{-7}	> 1	10^{+12}_{-8}
χ^2	51	52	75	58	81	58	48	55	75
ν	67	70	70	70	67	67	68	65	66
χ^2_{ν}	0.76	0.75	1.07	0.82	1.20	0.86	0.70	0.85	1.14

NOTE—The disk normalization is given by $N_{\text{disk}} = (R_{\text{in}}/D_{10})^2 \cos \theta$, where R_{in} is the apparent inner disk in km, D_{10} is the distance to the source in units of 10 kpc, and θ is the disk inclination. The total χ^2 is shown for each fit, along with the degrees of freedom, ν , and the reduced χ^2 , $\chi^2_\nu = \chi^2/\nu$. The ionization, $\log \xi$, is given by $L_{\text{irr}}/n_e R^2$, where L_{irr} is the ionizing luminosity, n_e is the gas density, and R is the distance to the ionizing source. N_{refl} is the normalization of the reflection component, **reflionxHD**. All other parameters are as described in the text.

García, J., Dauser, T., Reynolds, C. S., et al. 2013, ApJ, 768, 146, doi: [10.1088/0004-637X/768/2/146](https://doi.org/10.1088/0004-637X/768/2/146)

García, J., & Kallman, T. R. 2010, ApJ, 718, 695, doi: [10.1088/0004-637X/718/2/695](https://doi.org/10.1088/0004-637X/718/2/695)

García, J., Dauser, T., Lohfink, A., et al. 2014, ApJ, 782, 76, doi: [10.1088/0004-637X/782/2/76](https://doi.org/10.1088/0004-637X/782/2/76)

García, J. A., Grinberg, V., Steiner, J. F., et al. 2016, ApJ, 819, 76, doi: [10.3847/0004-637X/819/1/76](https://doi.org/10.3847/0004-637X/819/1/76)

García, J. A., Kallman, T. R., Bautista, M., et al. 2018, in Astronomical Society of the Pacific Conference Series, Vol. 515, Workshop on Astrophysical Opacities, 282

García, J. A., McClintock, J. E., Steiner, J. F., Remillard, R. A., & Grinberg, V. 2014, ApJ, 794, 73, doi: [10.1088/0004-637X/794/1/73](https://doi.org/10.1088/0004-637X/794/1/73)

García, J. A., Steiner, J. F., McClintock, J. E., et al. 2015, ApJ, 813, 84, doi: [10.1088/0004-637X/813/2/84](https://doi.org/10.1088/0004-637X/813/2/84)

García, J. A., Kara, E., Walton, D., et al. 2019, ApJ, 871, 88, doi: [10.3847/1538-4357/aaf739](https://doi.org/10.3847/1538-4357/aaf739)

Gatuzz, E., Díaz Trigo, M., Miller-Jones, J. C. A., & Migliari, S. 2019, MNRAS, 482, 2597, doi: [10.1093/mnras/sty2850](https://doi.org/10.1093/mnras/sty2850)

Gehrels, N., Chincarini, G., Giommi, P., et al. 2004, ApJ, 611, 1005, doi: [10.1086/422091](https://doi.org/10.1086/422091)

Table 6. Maximum likelihood estimates of all parameters in spectral fitting of *RXTE*-PCA observations of the 2002–2004 outburst of 4U 1630–47 with models (a) and (b). Model (a) enforces a fixed low-density reflection component ($n_e = 10^{15} \text{ cm}^{-3}$), and model (b) has a variable disk density with $n_e \leq 10^{22} \text{ cm}^{-3}$.

Parameter	Hardness Ratio								
	0.63	0.62	0.60	0.53	0.48	0.36	0.27	0.21	0.13
$R_{\text{in}} [R_{\text{ISCO}}]$					1				
a_*					0.998				
$i [^\circ]$					64				
A_{Fe}					5				
$N_{\text{H}} [10^{22} \text{ cm}^{-2}]$					14				
Model (a): TBabs(simplcut⊗diskbb+relconvlp⊗reflionx)									
Γ	$2.279^{+0.008}_{-0.006}$	$2.301^{+0.004}_{-0.002}$	$2.749^{+0.003}_{-0.003}$	$2.86^{+0.08}_{-0.12}$	$2.74^{+0.06}_{-0.04}$	$2.6^{+0.1}_{-0.6}$	> 2.4
f_{sc}	$0.4^{+0.6}_{-0.2}$	unconstrained	$0.868^{+0.007}_{-0.096}$	$0.51^{+0.05}_{-0.39}$	$0.24^{+0.03}_{-0.02}$	$0.10^{+0.04}_{-0.08}$	< 0.01
$T_{\text{in}} [\text{keV}]$	$0.29^{+0.02}_{-0.01}$	$0.762^{+0.007}_{-0.022}$	$0.904^{+0.004}_{-0.093}$	$1.222^{+0.017}_{-0.009}$	$1.424^{+0.004}_{-0.008}$	$1.362^{+0.016}_{-0.008}$	$1.243^{+0.006}_{-0.016}$
$kT_e [\text{keV}]$	$14.0^{+1.1}_{-0.4}$	$11.9^{+0.3}_{-0.3}$	> 220	> 100	> 100	< 300	< 14
$N_{\text{disk}} [10^2]$	6400^{+1277}_{-200}	62^{+32}_{-7}	$41.2^{+16.2}_{-0.4}$	9^{+3}_{-3}	$4.27^{+0.11}_{-0.06}$	$3.7^{+0.2}_{-0.2}$	$3.6^{+0.2}_{-0.1}$
$h [R_g]$	40^{+10}_{-20}	6^{+5}_{-2}	48^{+3}_{-3}	6^{+3}_{-2}	< 40	< 40	< 50
$\log \xi [\text{erg cm s}^{-1}]$	> 4.5	$3.3^{+0.4}_{-0.3}$	$4.03^{+0.11}_{-0.08}$	$4.1^{+0.6}_{-0.7}$	< 2.6	< 4.6	$2.0^{+0.3}_{-0.3}$
$N_{\text{refl}} [10^3]$	$0.05^{+0.38}_{-0.03}$	3^{+12}_{-2}	$0.078^{+0.009}_{-0.007}$	$4.4^{+5.8}_{-0.1}$	< 80	< 0.4	200^{+700}_{-100}
$n_e [\text{cm}^{-3}]$					10^{15}				
Strength _{abs}	$0.017^{+0.008}_{-0.007}$	$0.030^{+0.015}_{-0.009}$	$0.4^{+2.3}_{-0.3}$	$0.3^{+0.5}_{-0.2}$
χ^2	78	66	81	98	83	34	33
ν	62	63	61	60	54	43	33
χ^2_ν	1.25	1.05	1.33	1.64	1.54	0.79	1.01
Model (b): TBabs(simplcut⊗diskbb+relconvlp⊗reflionxHD)									
Γ	$2.19^{+0.12}_{-0.02}$	$2.22^{+0.01}_{-0.01}$	$2.16^{+0.08}_{-0.02}$	$2.53^{+0.06}_{-0.08}$	$2.615^{+0.003}_{-0.003}$	$2.47^{+0.03}_{-0.02}$	$2.37^{+0.08}_{-0.03}$	> 2.2	> 2.7
f_{sc}	$0.19^{+0.28}_{-0.06}$	$0.18^{+0.14}_{-0.02}$	< 0.8	< 0.9	$0.78^{+0.05}_{-0.69}$	< 0.05	< 0.04	$0.12^{+0.01}_{-0.05}$	< 0.01
$T_{\text{in}} [\text{keV}]$	$0.30^{+0.31}_{-0.01}$	$0.128^{+0.032}_{-0.004}$	$1.05^{+0.01}_{-0.04}$	$1.05^{+0.04}_{-0.05}$	$0.938^{+0.008}_{-0.008}$	$1.20^{+0.02}_{-0.02}$	$1.403^{+0.008}_{-0.012}$	$1.368^{+0.013}_{-0.009}$	$1.243^{+0.007}_{-0.007}$
$kT_e [\text{keV}]$	$12.2^{+0.7}_{-1.2}$	$12.1^{+0.8}_{-0.6}$	$13.2^{+0.4}_{-0.7}$	21^{+6}_{-4}	34^{+2}_{-2}	> 100	> 50	< 300	< 140
$N_{\text{disk}} [10^2]$	8000^{+8000}_{-2000}	42000^{+10340}_{-1000}	$7.8^{+10.1}_{-0.3}$	12^{+68}_{-5}	$29.2^{+0.4}_{-0.4}$	$6.3^{+0.3}_{-0.4}$	$3.60^{+0.11}_{-0.07}$	$3.7^{+0.1}_{-0.3}$	$3.55^{+0.11}_{-0.09}$
$h [R_g]$	< 3	< 20	26^{+18}_{-8}	13^{+11}_{-4}	$4.1^{+0.3}_{-0.3}$	7^{+9}_{-4}	> 3	< 60	< 23
$\log \xi [\text{erg cm s}^{-1}]$	> 4.5	$3.99^{+0.36}_{-0.05}$	$4.44^{+0.11}_{-0.05}$	$4.4^{+0.2}_{-0.2}$	$4.10^{+0.07}_{-0.07}$	$4.47^{+0.06}_{-0.07}$	> 4.6	< 3.3	< 1.5
N_{refl}	30^{+6}_{-15}	$1.8^{+0.6}_{-0.8}$	$7.5^{+0.8}_{-1.6}$	8^{+13}_{-1}	$8.4^{+63.1}_{-0.5}$	$4.7^{+1.3}_{-0.4}$	$1.28^{+0.59}_{-0.09}$	< 170	30^{+110}_{-20}
$n_e [10^{20} \text{ cm}^{-3}]$	$0.2^{+11.0}_{-0.1}$	> 10	> 60	> 40	$0.72^{+0.08}_{-0.08}$	10^{+32}_{-4}	10^{+9}_{-4}	< 100	> 10
Strength _{abs}	$0.009^{+0.009}_{-0.007}$	$0.025^{+0.012}_{-0.009}$	$0.2^{+0.6}_{-0.1}$	$0.16^{+0.24}_{-0.08}$
χ^2	73	46	100	64	47	71	72	33	29
ν	61	62	62	62	60	59	53	42	32
χ^2_ν	1.20	0.74	1.61	1.03	0.78	1.21	1.35	0.79	0.92

NOTE—The disk normalization is given by $N_{\text{disk}} = (R_{\text{in}}/D_{10})^2 \cos \theta$, where R_{in} is the apparent inner disk in km, D_{10} is the distance to the source in units of 10 kpc, and θ is the disk inclination. The total χ^2 is shown for each fit, along with the degrees of freedom, ν , and the reduced χ^2 , $\chi^2_\nu = \chi^2/\nu$. The ionization, $\log \xi$, is given by $L_{\text{irr}}/n_e R^2$, where L_{irr} is the ionizing luminosity, n_e is the gas density, and R is the distance to the ionizing source. N_{refl} is the normalization of the reflection component, **reflionxHD**. Strength_{abs} is the strength of the Gaussian absorption line, with centroid energy $E_{\text{abs}} = 6.9 \text{ keV}$, and width $\sigma_{\text{abs}} = 10 \text{ eV}$, both frozen parameters. All other parameters are as described in the text. Observations 80117-01-03-00G (HR = 0.60) and 80117-01-07-01 (HR = 0.53) are not included in Model (a) spectral fitting results due to poor fits, and thus unreliable parameter constraints.

Harrison, F. A., Craig, W. W., Christensen, F. E., et al. 2013, *Astrophys. J.*, 770, 103,

doi: [10.1088/0004-637X/770/2/103](https://doi.org/10.1088/0004-637X/770/2/103)

Higginbottom, N., Knigge, C., Sim, S. A., et al. 2020, *MNRAS*, 492, 5271, doi: [10.1093/mnras/staa209](https://doi.org/10.1093/mnras/staa209)

Homan, J., & Belloni, T. 2005, *Ap&SS*, 300, 107, doi: [10.1007/s10509-005-1197-4](https://doi.org/10.1007/s10509-005-1197-4)

Hori, T., Ueda, Y., Done, C., Shidatsu, M., & Kubota, A. 2018, *ApJ*, 869, 183, doi: [10.3847/1538-4357/aad5e](https://doi.org/10.3847/1538-4357/aad5e)

Hori, T., Ueda, Y., Shidatsu, M., et al. 2014, *ApJ*, 790, 20, doi: [10.1088/0004-637X/790/1/20](https://doi.org/10.1088/0004-637X/790/1/20)

Jahoda, K., Swank, J. H., Giles, A. B., et al. 1996, in *Society of Photo-Optical Instrumentation Engineers (SPIE) Conference Series*, Vol. 2808, EUV, X-Ray, and Gamma-Ray Instrumentation for Astronomy VII, ed. O. H. Siegmund & M. A. Gummin, 59–70

Jiang, J., Fabian, A. C., Wang, J., et al. 2019a, *MNRAS*, 484, 1972, doi: [10.1093/mnras/stz095](https://doi.org/10.1093/mnras/stz095)

- Jiang, J., Fabian, A. C., Dauser, T., et al. 2019b, *MNRAS*, 489, 3436, doi: [10.1093/mnras/stz2326](https://doi.org/10.1093/mnras/stz2326)
- Kalemci, E., Maccarone, T. J., & Tomsick, J. A. 2018, *ApJ*, 859, 88, doi: [10.3847/1538-4357/aabcd3](https://doi.org/10.3847/1538-4357/aabcd3)
- Kallman, T., & Bautista, M. 2001, *ApJS*, 133, 221, doi: [10.1086/319184](https://doi.org/10.1086/319184)
- King, A. L., Walton, D. J., Miller, J. M., et al. 2014, *ApJL*, 784, L2, doi: [10.1088/2041-8205/784/1/L2](https://doi.org/10.1088/2041-8205/784/1/L2)
- Kolehmainen, M., Done, C., & Díaz Trigo, M. 2011, *MNRAS*, 416, 311, doi: [10.1111/j.1365-2966.2011.19040.x](https://doi.org/10.1111/j.1365-2966.2011.19040.x)
- Krimm, H. A., Holland, S. T., Corbet, R. H. D., et al. 2013, *ApJS*, 209, 14, doi: [10.1088/0067-0049/209/1/14](https://doi.org/10.1088/0067-0049/209/1/14)
- Kubota, A., Tanaka, Y., Makishima, K., et al. 1998, *PASJ*, 50, 667, doi: [10.1093/pasj/50.6.667](https://doi.org/10.1093/pasj/50.6.667)
- Kubota, A., Dotani, T., Cottam, J., et al. 2007, *PASJ*, 59, 185, doi: [10.1093/pasj/59.sp1.S185](https://doi.org/10.1093/pasj/59.sp1.S185)
- Kuulkers, E., Wijnands, R., Belloni, T., et al. 1998, *ApJ*, 494, 753, doi: [10.1086/305248](https://doi.org/10.1086/305248)
- Lasota, J.-P. 2001, *NewAR*, 45, 449, doi: [10.1016/S1387-6473\(01\)00112-9](https://doi.org/10.1016/S1387-6473(01)00112-9)
- McClintock, J. E., Shafee, R., Narayan, R., et al. 2006, *ApJ*, 652, 518, doi: [10.1086/508457](https://doi.org/10.1086/508457)
- Miller, J. M., Raymond, J., Reynolds, C. S., et al. 2008, *ApJ*, 680, 1359, doi: [10.1086/588521](https://doi.org/10.1086/588521)
- Mitsuda, K., Inoue, H., Koyama, K., et al. 1984, *PASJ*, 36, 741
- Novikov, I. D., & Thorne, K. S. 1973, in *Black Holes (Les Astres Occlus)*, ed. C. Dewitt & B. S. Dewitt, 343–450
- Ponti, G., Fender, R. P., Begelman, M. C., et al. 2012, *MNRAS*, 422, L11, doi: [10.1111/j.1745-3933.2012.01224.x](https://doi.org/10.1111/j.1745-3933.2012.01224.x)
- Priedhorsky, W. 1986, *Ap&SS*, 126, 89, doi: [10.1007/BF00644177](https://doi.org/10.1007/BF00644177)
- Reis, R. C., Fabian, A. C., Ross, R. R., et al. 2008, *MNRAS*, 387, 1489, doi: [10.1111/j.1365-2966.2008.13358.x](https://doi.org/10.1111/j.1365-2966.2008.13358.x)
- Remillard, R. A., & McClintock, J. E. 2006, *ARA&A*, 44, 49, doi: [10.1146/annurev.astro.44.051905.092532](https://doi.org/10.1146/annurev.astro.44.051905.092532)
- Romano, P., Moretti, A., Banat, P. L., et al. 2006, *A&A*, 450, 59, doi: [10.1051/0004-6361:20054172](https://doi.org/10.1051/0004-6361:20054172)
- Ross, R. R., & Fabian, A. C. 2005, *MNRAS*, 358, 211, doi: [10.1111/j.1365-2966.2005.08797.x](https://doi.org/10.1111/j.1365-2966.2005.08797.x)
- . 2007, *MNRAS*, 381, 1697, doi: [10.1111/j.1365-2966.2007.12339.x](https://doi.org/10.1111/j.1365-2966.2007.12339.x)
- Seifina, E., Titarchuk, L., & Shaposhnikov, N. 2014, *ApJ*, 789, 57, doi: [10.1088/0004-637X/789/1/57](https://doi.org/10.1088/0004-637X/789/1/57)
- Shakura, N. I., & Sunyaev, R. A. 1973, *A&A*, 24, 337
- Smith, R. K., Valencic, L. A., & Corrales, L. 2016, *ApJ*, 818, 143, doi: [10.3847/0004-637X/818/2/143](https://doi.org/10.3847/0004-637X/818/2/143)
- Sridhar, N., García, J. A., Steiner, J. F., et al. 2020, *ApJ*, 890, 53, doi: [10.3847/1538-4357/ab64f5](https://doi.org/10.3847/1538-4357/ab64f5)
- Steiner, J. F., García, J. A., Eikmann, W., et al. 2017, *ApJ*, 836, 119, doi: [10.3847/1538-4357/836/1/119](https://doi.org/10.3847/1538-4357/836/1/119)
- Steiner, J. F., McClintock, J. E., Remillard, R. A., et al. 2010, *ApJ*, 718, L117, doi: [10.1088/2041-8205/718/2/L117](https://doi.org/10.1088/2041-8205/718/2/L117)
- Steiner, J. F., McClintock, J. E., Remillard, R. A., Narayan, R., & Gou, L. 2009a, *ApJL*, 701, L83, doi: [10.1088/0004-637X/701/2/L83](https://doi.org/10.1088/0004-637X/701/2/L83)
- Steiner, J. F., Narayan, R., McClintock, J. E., & Ebisawa, K. 2009b, *PASP*, 121, 1279, doi: [10.1086/648535](https://doi.org/10.1086/648535)
- Tetarenko, B. E., Sivakoff, G. R., Heinke, C. O., & Gladstone, J. C. 2016, *ApJS*, 222, 15, doi: [10.3847/0067-0049/222/2/15](https://doi.org/10.3847/0067-0049/222/2/15)
- Tomsick, J. A., Corbel, S., Goldwurm, A., & Kaaret, P. 2005, *ApJ*, 630, 413, doi: [10.1086/431896](https://doi.org/10.1086/431896)
- Tomsick, J. A., & Kaaret, P. 2000, *ApJ*, 537, 448, doi: [10.1086/308999](https://doi.org/10.1086/308999)
- Tomsick, J. A., Lapshov, I., & Kaaret, P. 1998, *ApJ*, 494, 747, doi: [10.1086/305240](https://doi.org/10.1086/305240)
- Tomsick, J. A., Parker, M. L., García, J. A., et al. 2018, *ApJ*, 855, 3, doi: [10.3847/1538-4357/aaaab1](https://doi.org/10.3847/1538-4357/aaaab1)
- Toor, A., & Seward, F. D. 1974, *AJ*, 79, 995, doi: [10.1086/111643](https://doi.org/10.1086/111643)
- Verner, D. A., Ferland, G. J., Korista, K. T., & Yakovlev, D. G. 1996, *ApJ*, 465, 487, doi: [10.1086/177435](https://doi.org/10.1086/177435)
- Wang-Ji, J., García, J. A., Steiner, J. F., et al. 2018, *ApJ*, 855, 61, doi: [10.3847/1538-4357/aaa974](https://doi.org/10.3847/1538-4357/aaa974)
- Wilkins, D. R., García, J. A., Dauser, T., & Fabian, A. C. 2020, *MNRAS*, doi: [10.1093/mnras/staa2566](https://doi.org/10.1093/mnras/staa2566)
- Wilms, J., Allen, A., & McCray, R. 2000, *ApJ*, 542, 914, doi: [10.1086/317016](https://doi.org/10.1086/317016)
- Zdziarski, A., De Marco, B., Szanecki, M., & Markowitz, A. 2020, arXiv e-prints, arXiv:2006.12829, <https://arxiv.org/abs/2006.12829>
- Zdziarski, A. A., & De Marco, B. 2020, *ApJL*, 896, L36, doi: [10.3847/2041-8213/ab9899](https://doi.org/10.3847/2041-8213/ab9899)
- Zdziarski, A. A., Johnson, W. N., & Magdziarz, P. 1996, *MNRAS*, 283, 193, doi: [10.1093/mnras/283.1.193](https://doi.org/10.1093/mnras/283.1.193)
- Życki, P. T., Done, C., & Smith, D. A. 1999, *MNRAS*, 309, 561, doi: [10.1046/j.1365-8711.1999.02885.x](https://doi.org/10.1046/j.1365-8711.1999.02885.x)